



3 1293 10065 8685



This is to certify that the

thesis entitled

Microstructural Aspects of Impact Erosion
in LiF, NaCl, KCl, and CaF₂ Single Crystals

presented by

Susan Roberta Schuon

has been accepted towards fulfillment
of the requirements for

Ph.D. degree in Metallurgy

S. N. Abrahamian

Major professor

Date February 21, 1980



OVERDUE FINES:
25¢ per day per item

RETURNING LIBRARY MATERIALS:
Place in book return to remove
charge from circulation records

306-186 82 90	
309-829 132	
CB	
306-161	

MICROSTRUCTURAL ASPECTS OF IMPACT EROSION IN
LiF, NaCl, KCl, AND CaF₂ SINGLE CRYSTALS

by

Susan Roberta Schuon

A DISSERTATION

Submitted to

Michigan State University

in partial fulfillment of the requirements

for the degree of

DOCTOR OF PHILOSOPHY

Department of Metallurgy, Mechanics, and Materials Science

1980

ABSTRACT

MICROSTRUCTURAL ASPECTS OF IMPACT EROSION IN

LiF, NaCl, KCl, AND CaF₂ SINGLE CRYSTALS

by

Susan Roberta Schuon

In an attempt to clarify the fundamental mechanism of material removal in erosion by solid particles entrained in a fluid stream impinging on a solid surface, single crystals were selected for targets in view of their precisely-defined structure. The target materials were CaF₂ (relatively brittle), LiF (intermediate between brittle and ductile) and KCl and NaCl (relatively ductile). The impinging particles were 0.25 mm glass beads (blunt), 0.50 mm quartz sand grains (blunt), and 0.175 mm SiC particles (sharp). The velocity of the particles, which were entrained in a moving stream of dry nitrogen, was varied between 2 m/s and 120 m/s. In most of the experiments, the gas stream was directed normally on selected crystal planes of the target materials. Experiments were conducted at room temperature (25°C) on all targets, and at 200°C and 400°C on LiF. The damage to the target by impact of a single particle ("single-impact mode") and by impact of a stream of particles ("multiple-impact mode") was studied by scanning electron microscopy. In addition, the damage by multiple impact was assessed by measuring the erosion rate.

In the single-impact mode, the damage is highly dependent on the mechanical properties of the target as chips spalled off or micro-machined out in individual impacts, or as chips produced upon the

intersection of fractures resulting from several neighboring impacts which in themselves would not have caused erosion. Which mechanism is predominant, or even present, is controlled primarily by the shape of the projectile and the ductility of the target, and secondarily by the projectile size, the direction and magnitude of projectile velocity, the target hardness, and the orientation of active slip planes in the target. At normal impact, the predominant mechanism is intersecting fractures, but at impact angles away from the normal, micromachining appears in NaCl and KCl, and in fact becomes the major mechanism of material removal. In LiF, only a little micromachining occurs and in CaF₂, none at all; hence in these materials, spalling is the controlling mechanism for loss in individual impacts.

To
My parents and grandparents

ACKNOWLEDGEMENTS

I would like to express my deepest gratitude to the following people:

my advisor, Dr. K. N. Subramanian, for his guidance and help throughout my graduate studies;

my graduate committee, Dr. Nicholas Altiero, Dr. Carl Foiles, and especially Dr. Donald J. Montgomery, for their review and advice;

the faculty and staff of the MMM Department, especially Dr. John Martin for his help, and the late Dr. Denton McGrady for his guidance and wisdom;

Dr. Robert Summitt for his friendship and support;

Mrs. Thelma Liszewski for her advice and typing of this thesis;

Dr. Leroy Dugan and the Graduate Council for their encouragement and approval of my program;

my Geology graduate committee, Dr. F. W. Cambray, Dr. James Trow, Dr. John Wilband, and Dr. Hugh Bennett, for their understanding;

my parents, Robert and Leona Schuon, and my grandparents, Earl and Margaret Schuon and Stanley and Maria Stanish, for their faith and support;

Dr. George Van Dusen and the student services staff for their encouragement;

and finally, my fellow graduate students, especially Sudhira, Ali, Dave, Abdul, Candy, Sue, Ben, and Greg, for their encouragement and friendship when things looked the darkest.

TABLE OF CONTENTS

	Page
LIST OF TABLES	vi
LIST OF FIGURES	vii
 Chapter	
I. INTRODUCTION	1
1.1 Crystal Structure and Slip Systems in Crystals of NaCl Structure and Fluorite Structure	2
1.2 Theories of Erosion	5
1.3 Objectives	16
II. EXPERIMENTAL PROCEDURE	17
2.1 Sample Preparation	17
2.2 Impact Erosion Experiments	18
2.2.1 Projectiles	18
2.2.2 Low-Temperature Testing	18
2.2.3 High-Temperature Testing	23
2.3 Microscopic Analysis	23
2.3.1 Etchants	23
2.3.2 Scanning Electron Microscopy	25
2.3.3 Microprobe Analysis	25
III. RESULTS AND DISCUSSION	27
3.1 Single Impact Damage Produced by Blunt Projectiles	27
3.1.1 Low-Temperature Slip and Crack Nucleation at Normal Impact on the Cleavage Plane	27
3.1.2 Normal Impact Erosion at Elevated Tempera- tures in LiF on the Cleavage Plane	44
3.1.3 Slip and Crack Nucleation in NaCl-Structure Crystals on the {110} and {111} Planes at Normal Impact	48
3.1.4 Slip and Crack Nucleation at Angles of Impact on the Cleavage Plane Other Than 90°	50
3.1.5 The Relationship of Blunt-Projectile Damage to the Hertzian Stress Field	62
3.1.6 Impact Damage Produced by Sharp Projectiles	64

	Page
3.2 Multiple-Impact Damage	70
3.2.1 Impact-Erosion Damage Produced by Multiple Blunt-Projectile Impact	73
3.2.2 Impact-Erosion Damage Produced by Multiple Sharp-Projectile Impact	81
IV. CONCLUSIONS	90
APPENDIX	149
A. Tables	149
LIST OF REFERENCES	158

LIST OF TABLES

Table	Page
A.1 Diameter of the zone of contact and the length of lateral fractures in crystals eroded by 0.25 mm glass beads impacting the {001} in NaCl, KCl, LiF and the {111} in CaF ₂ . (counts/sample = 10)	149
A.2 Diameter of the zone of contact versus the velocity of 0.25 mm glass beads impacting the {001} in NaCl, KCl, and LiF and the {111} in CaF ₂ . (counts/sample = 10)	150
A.3 Diameter of the zone of contact versus the velocity of 0.50 mm blunt projectiles impacting the {001} in NaCl, KCl, and LiF and the {111} in CaF ₂ . (counts/sample = 10)	151
A.4 Diameter of the zone of contact versus the velocity calculated using Hertz's analysis for contact of a spherical indenter on an isotropic medium	152
A.5 The rate of erosion versus the impact velocity of 0.25 mm glass beads impacting the {001} in NaCl, KCl, and LiF and {111} in CaF ₂	153
A.6 The rate of erosion versus the impact velocity of 0.50 mm blunt projectiles impacting the {001} in NaCl, KCl, and LiF and {111} in CaF ₂	154
A.7 The rate of erosion versus the impact velocity of 0.25 mm glass beads impacting the {001} in NaCl, KCl, and LiF and {111} in CaF ₂ at an angle 60° from an axis normal to surface of the crystal	155
A.8 The rate of erosion versus the impact velocity of 0.25 mm projectiles impacting the {110}	156
A.9 The rate of erosion versus the impact velocity of SiC powder impacting the {001} in NaCl, KCl, and LiF, and the {111} in CaF ₂	157

LIST OF FIGURES

Figure	Page
1. a. A unit cell of NaCl b. A unit cell of CaF ₂	3
2. Slip in NaCl-structure crystals a. {001}<110> system b. {110}<110> system	4
3. Rate of erosion versus time	6
4. Rate of erosion versus angle of impact	10
5. Impact stress field for: a. a Hertzian stress field (blunt-projectile impact) b. a Boussinesq stress field (sharp-projectile impact) . .	14
6. Particles used as projectiles for impact damage a. Glass beads b. Quartz sand c. SiC	19
7. Room-temperature test apparatus with jet-air abrasive device, sample holder and timing disc	20
8. Experimental set-up for velocity measurement at low temperatures a. Schematic b. Lower disc (x=stationary mark, y=dynamic mark) c. Upper disc with slit cut out	22
9. High-temperature apparatus with jet-air abrasive device, sample holder, and furnace	24
10. A scanning electron micrograph of CaF ₂ eroded by 0.25 mm glass beads impacting the {111} at a velocity of 2 m/s . .	29
11. A scanning electron micrograph of LiF eroded by 0.25 mm glass beads impacting the {001} at a velocity of 10 m/s (etched).	30
12. Orientation of the {001}, {101}, and {110} planes	31
13. A scanning electron micrograph of LiF eroded by 0.25 mm glass beads impacting the {001} at a velocity of 45 m/s (etched).	33

Figure	Page
14. Formation and reorientation of chips during impact	34
15. A scanning electron micrograph of KCl eroded by 0.25 mm glass beads impacting the {001} at a velocity of 25 m/s . . .	35
16. A scanning electron micrograph of CaF ₂ eroded by 0.25 mm glass beads impacting the {111}: a. at a velocity of 45 m/s b. at a velocity of 30 m/s (etched)	36
17. A scanning electron micrograph of CaF ₂ eroded by 0.25 mm glass beads impacting the {111} at a velocity of 30 m/s a. Single impact b. Double impact	37
18. A scanning electron micrograph of NaCl eroded by 0.25 mm glass beads impacting the {001} at a velocity of 25 m/s . . .	38
19. A scanning electron micrograph of LiF eroded by 0.50 mm blunt projectiles impacting the {001} at a velocity of 45 m/s (etched).	40
20. A scanning electron micrograph of LiF eroded by 0.25 mm glass beads impacting the {001} at a velocity of 45 m/s. The plane of observation is the {010}	41
21. A scanning electron micrograph of LiF eroded by 0.50 mm blunt projectiles impacting the {001} at a velocity of 35 m/s (etched)	43
22. A scanning electron micrograph of CaF ₂ eroded by 0.25 mm glass beads impacting the {111} at a velocity of 15 m/s (etched)	45
23. A scanning electron micrograph of LiF eroded at 200°C by 0.50 mm blunt projectiles impacting the {001}: a. at an angle 90° from the crystal surface at a velocity of 45 m/s b. at an angle 60° from the crystal surface at a velocity of 45 m/s (etched)	46
24. A scanning electron micrograph of LiF eroded at 200°C by blunt projectiles impacting the {001} at a velocity of 45/ms (etched) ("b" is part of "a")	47
25. A scanning electron micrograph of LiF eroded at 400°C by 0.50 mm blunt projectiles impacting the {001}: a. at a velocity of 45 m/s b. at a velocity of 60 m/s (etched)	49

Figure	Page
26. A scanning electron micrograph of:	
a. LiF eroded by 0.50 mm blunt projectiles impacting the {110} at a velocity of 45 m/s	
b. NaCl eroded by 0.50 mm blunt projectiles impacting the {110} at a velocity of 45 m/s	51
27. A scanning electron micrograph of:	
a. KCl eroded by 0.50 mm blunt projectiles impacting the {110} at a velocity of 75 m/s	
b. NaCl eroded by 0.50 mm blunt projectiles impacting the {110} at a velocity of 60 m/s	52
28. A scanning electron micrograph of:	
a. LiF eroded by 0.50 mm blunt projectiles impacting the {111} at a velocity of 45 m/s	
b. KCl eroded by 0.50 mm blunt projectiles impacting the {111} at a velocity of 45 m/s	53
29. A scanning electron micrograph of 0.50 mm blunt projectiles impacting the {111} at a velocity of 45 m/s ("a" is the area of contact of "b")	54
30. a. The orientation of slip planes in NaCl structure crystals with respect to the direction of impact on the {110}	
b. The orientation of slip planes in NaCl structure crystals with respect to the direction of impact on the {111}	55
31. A scanning electron micrograph of KCl eroded by 0.25 mm glass beads impacting the {001} at an angle 60° from an axis normal to the surface of the crystal at a velocity of 10 m/s	57
32. A scanning electron micrograph of KCl eroded by 0.25 mm glass beads impacting the {001} at an angle 60° from an axis normal to the surface of the crystal at a velocity of 10 m/s	58
33. A scanning electron micrograph of LiF eroded using 0.50 mm blunt projectiles impacting the {001}:	
a. at an angle 30° from an axis normal to the surface of the crystal at a velocity of 25 m/s	
b. at an angle 60° from an axis normal to the surface of the crystal at a velocity of 35 m/s	59
34. A scanning electron micrograph of CaF ₂ eroded by 0.50 mm blunt projectiles impacting the {111} at an angle 60° from an axis normal to the surface of the crystal:	
a. at a velocity of 20 m/s	
b. at a velocity of 45 m/s (etched)	61

Figure	Page
35. The diameter of the circle of contact versus the length of the lateral fractures	63
36. The diameter of the circle of contact versus the velocity of impact of 0.25 mm glass beads	65
37. The diameter of the circle of contact versus the impact velocity of 0.50 mm blunt projectiles	66
38. The diameter of the circle of contact calculated using Hertz's analysis for contact of a spherical indenter on an isotropic medium versus the impact velocity (D=diameter of the projectile)	67
39. Possible modes of specimen loading by sharp projectiles impacting the surface of the crystals a. Point b. Edge c. Side	68
40. A scanning electron micrograph of LiF eroded by sharp projectiles impacting the {001} at a velocity of 45 m/s . .	69
41. A scanning electron micrograph of LiF eroded by sharp projectiles impacting the {001}: a. at a velocity of 20 m/s b. at a velocity of 45 m/s	71
42. A scanning electron micrograph of CaF ₂ eroded by sharp projectiles impacting the {111} at a velocity of 45 m/s . .	72
43. A scanning electron micrograph of CaF ₂ eroded by 0.25 mm glass beads impacting the {001} at a velocity of 25 m/s . .	74
44. A scanning electron micrograph of LiF eroded by 0.25 mm glass beads impacting the {001} at a velocity of 45 m/s . .	75
45. A scanning electron micrograph of KCl eroded by 0.25 mm glass beads impacting the {001} at a velocity of 75 m/s . .	77
46. A scanning electron micrograph of CaF ₂ eroded by 0.25 mm glass beads impacting the {111} at a velocity of 75 m/s . .	78
47. The rate of erosion versus the impact velocity of 0.25 mm projectiles impacting the {001} in NaCl, KCl and LiF, and the {111} in CaF ₂	79
48. The rate of erosion versus the impact velocity of 0.50 mm projectiles impacting the {001} in NaCl, KCl, and LiF, and the {111} in CaF ₂	80

Figure	Page
49. A scanning electron micrograph of KCl eroded by 0.25 mm glass beads impacting the {001} at a velocity of 75 m/s . . .	82
50. A scanning electron micrograph of KCl eroded by 0.25 mm glass beads impacting the {001} at a velocity of 75 m/s . . .	83
51. The rate of erosion versus the impact velocity of 0.25 mm projectiles impacting the {001} in NaCl, KCl, and LiF, and {111} in CaF ₂ at an angle of 60° from an axis normal to the surface of the crystal	84
52. The rate of erosion versus the impact velocity of 0.25 mm projectiles impacting the {110}	85
53. A scanning electron micrograph of KCl eroded by 0.50 mm blunt projectiles impacting the {110} at a velocity of 75 m/s	86
54. A scanning electron micrograph of LiF eroded by 0.50 mm blunt projectiles impacting the {110} at a velocity of 75 m/s	87
55. The rate of erosion versus the impact velocity of SiC powder impacting the {001} in NaCl, KCl, and LiF, and the {111} in CaF ₂	89

1. INTRODUCTION

Erosion is an important industrial phenomenon. In any situation where solid particles are entrained in a gas or fluid, impact erosion can cause significant material loss. On the one hand, severe erosion produces material loss and mechanical degradation in petrochemical processing equipment, rocket nozzles, helicopter parts, and turbine blades. On the other hand, erosion by "sand blasting" often serves for machining ceramics and for removing scale. Studies of erosion by solid particles have generally fallen into two categories: those seeking to relate erosion weight loss to a simple property of the material, and those seeking an empirical test to establish relative erosion resistance of various materials.¹ In contrast, few studies have tried to determine the mechanisms of erosion.² In this study, the role of microscopic deformation in the erosion behavior of ductile and semi-ductile halide crystals will be investigated.

To gain a better understanding of the fundamental mechanisms of erosion, a simple material free of macroscopic flaws is desirable. Single crystals are ideal candidates, especially since grain boundaries have been shown to play only a minor role in cavitation erosion and not to form sites of preferential erosion.³ Therefore, single crystals are legitimate models for polycrystalline materials in erosion. In such crystals, moreover, it is possible to determine the fundamental mechanisms of erosion without the added effects of macroscopic

impurities or flaws. LiF, CaF₂, NaCl, and KCl single crystals were chosen because they have simple, well-known crystal structures and slip systems.

1.1 Crystal Structure and Slip Systems in Crystals of NaCl Structure and Fluorite Structure.

The NaCl structure is a nearly perfect example of ionic bonding with alternate lattice points occupied by anions and cations. The crystal structure may be described as a face-centered cubic arrangement with an Na⁺ Cl⁻ basis, the sodium cations occupying all of the octahedral sites as shown in Figure 1a. Most of the alkali halides have this structure. In contrast, the fluorite structure can be described as a face-centered cubic arrangement of calcium ions, with every other tetrahedral site filled with fluorine ions as shown in Figure 1b.⁴

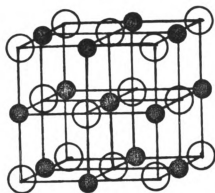
The mechanical behavior of NaCl-type crystals, (LiF, NaCl, and KCl) and CaF₂ has been extensively studied.⁵⁻¹² In NaCl-structure crystals at low temperatures, the {110} <1 $\bar{1}$ 0> slip system is preferred as a result of the strong repulsion between like ions (Figure 2a). At higher temperatures, thermal expansion renders this factor less important, and slip begins to occur on the {001} plane in the <110> direction (Figure 2b). NaCl-type crystals cleave readily along the {100} and less readily along the {110}.

In CaF₂ at low temperatures, slip has been observed on the {100} <011> family, and at elevated temperatures, on the {110} <1 $\bar{1}$ 0>. Cleavage occurs most readily on the {111} planes.

Fig. 1 a. A unit cell of NaCl.
b. A unit cell of CaF₂.

3 (a)

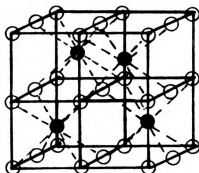
A



● Na

○ Cl

B



● Ca

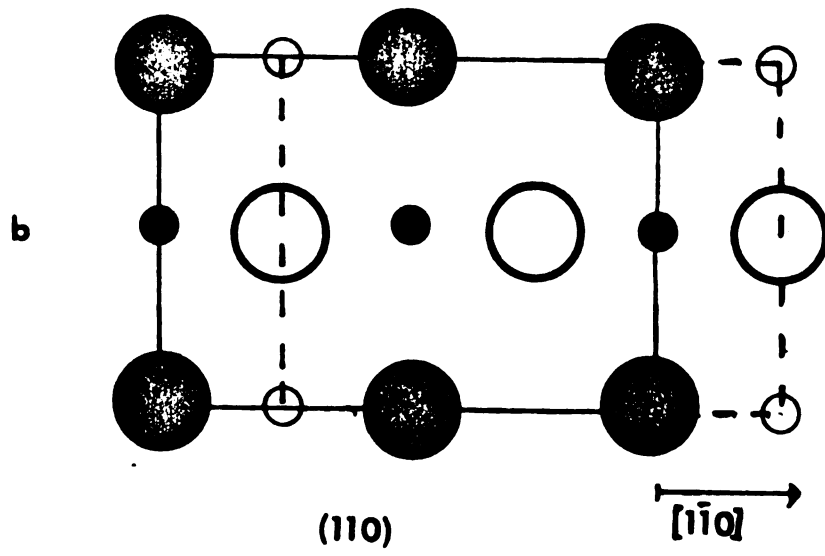
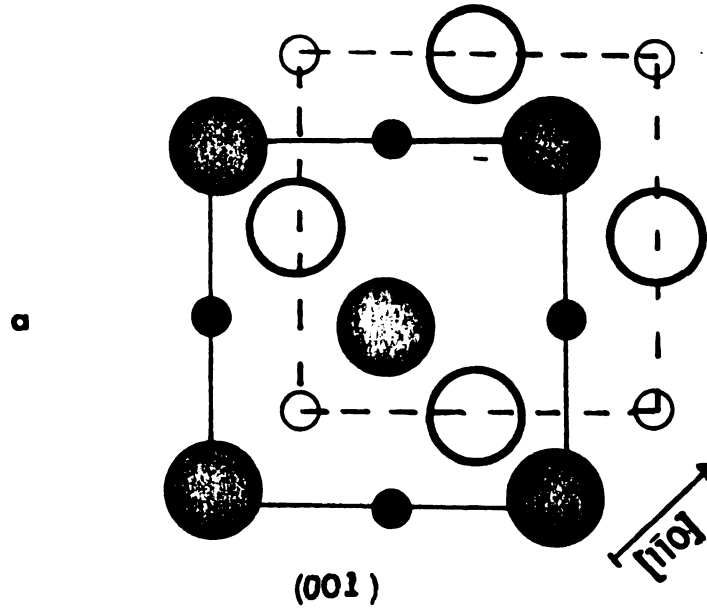
○ F

Fig. 2. Slip in NaCl structure crystals.

a. $\{001\}\langle 1\bar{1}0\rangle$ system.

b. $\{110\}\langle 1\bar{1}0\rangle$ system.

4(a)



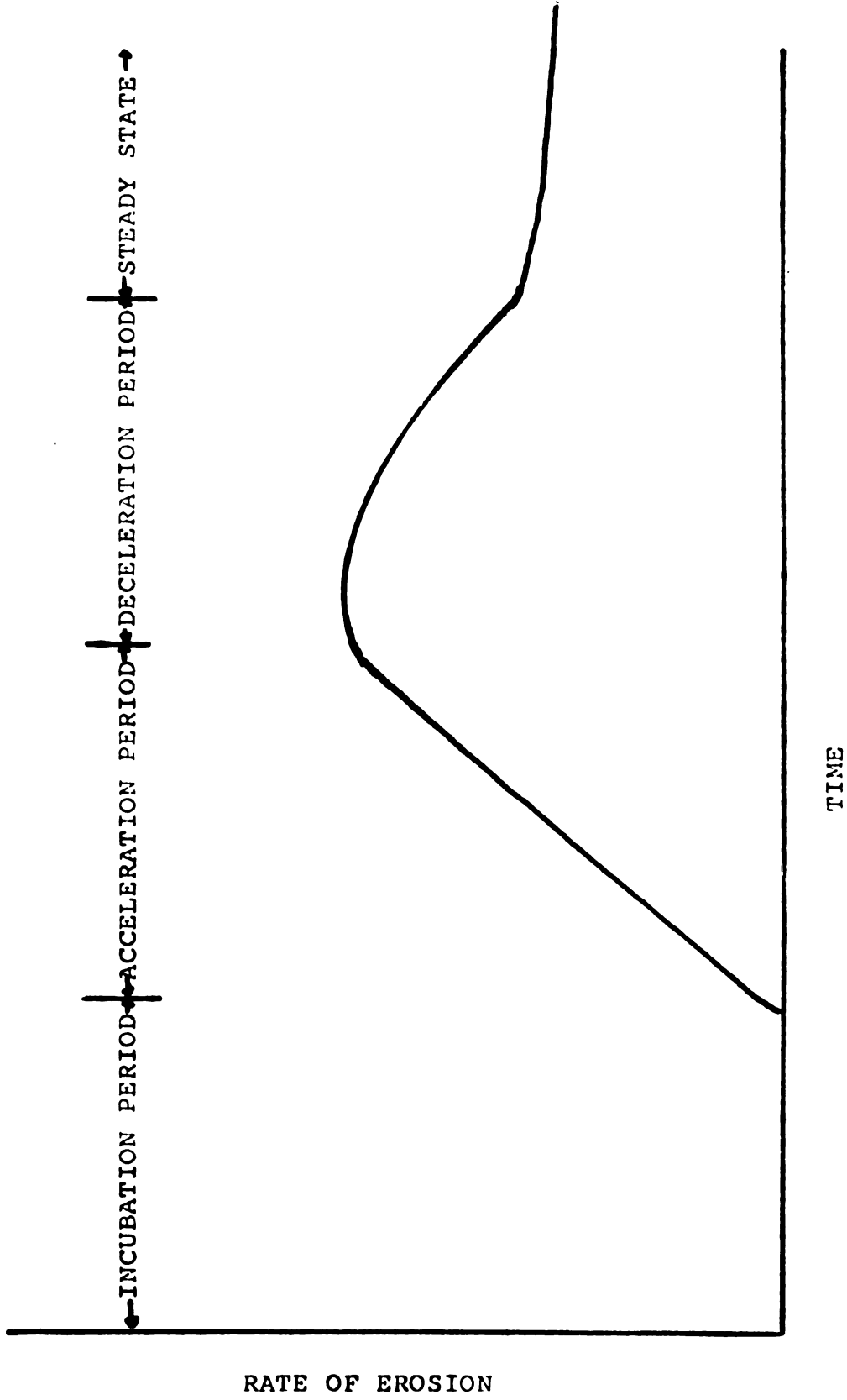
1.2 Theories of Erosion

Most studies of erosion have dealt with macroscopic behavior of complex industrial materials. Inasmuch as the present experiments deal with a fundamental study on special substances, an explanation of them cannot be expected to correspond with the explanation for earlier studies on less precisely defined systems. Nevertheless, a review of previous work is worthwhile in suggesting possible directions of interpretations.

Although caused by different processes, liquid-impact erosion, solid-impact erosion, and cavitation show many similarities in microstructural damage. Many authors have observed distinct periods of erosion, be it cavitation or impact erosion.¹³⁻¹⁹ Thiruvengadam¹³ has suggested that there are four distinct periods of erosion: the incubation period, acceleration period, deceleration period, and the steady-state period (cf. Figure 3). During the incubation period, the rate of erosion increases linearly with time. Many other investigators, in contrast with Thiruvengadam, do not observe a deceleration period. Plesset and Devine²⁰ attributed the presumed deceleration period to hydrodynamic damping effects due to the heavily roughened specimen surface. Also, these authors hold that there is no real indication of any final steady-state period. In brittle materials, Hoff et al.²¹ observed a critical velocity below which no erosion occurs. Above the critical velocity, ceramics and glasses fail rapidly owing to severe crack propagation. Metals--which erode at lower velocities--are more resistant above the critical velocity, as they can still deform before complete destruction. Therefore, Hoff et al.²¹ proposed that the

Fig. 3. Rate of erosion versus time.

6(a)



notch-impact strength be a criterion for the erosion resistance of brittle materials. Hockey et al.²² agreed.

Microstructural damage during the incubation period in ductile materials has been studied by Erdmann-Jesnitzer and Louis,²³ and Vyas and Preece.²⁴ Erdmann-Jesnitzer and Louis studied cavitation erosion in polycrystalline aluminum, iron, and zinc. Vyas and Preece studied cavitation erosion in aluminum bicrystals and polycrystalline aluminum. In both studies, massive plastic flow with evenly-spaced slip bands was observed in aluminum, though not in zinc; deformation twins, however, were observed around impressions on crystal surfaces. With longer time of loading, the size and the number of deformation twins increased. This increase was followed by transcrystalline cracking.

Some authors have proposed partial melting as a major mechanism of material removal.^{25,26} The rise in target temperature upon impact, ΔT , can be calculated from:²⁷

$$\Delta T = \frac{0.0212\alpha^{0.5} (1-e^2) E_r^{0.6} m^{0.4} v^{1.3}}{k R^{0.7}} \quad (1)$$

where k = thermal conductivity, (k cal/cm-sec- $^{\circ}$ C)

e = coefficient of restitution,

E_r = reduced modulus of elasticity, (N/m^2),

R = particle radius, (m),

α = thermal diffusivity, (watt/ mC°), and

v = particle velocity, (m/s).

Localized heat generation is very fast compared with heat conduction. Even so, in an example of the impact of a steel projectile (0.0012 Kg and 0.14 mm in diameter) on a steel surface, the rise in temperature at

the surface is only 1.47°C for a velocity of 1.73 m/s .²⁷ Other recent microstructural studies, as reviewed in reference 24, have questioned the effect of partial melting as a factor in erosion.

In oblique impact, micromachining has been proposed as a major mechanism of metal removal.²⁸⁻³¹ Finnie²⁸ proposed that each particle acts as a tool. During impact, material flows uniformly outward from the front and sides of the particle until the displaced material is strain hardened enough to fracture. Tilly²⁹ proposed a two-stage process of erosion in which the particle forms an indentation and a chip on the crystal surface, and then breaks up, the resulting fragments removing material by scouring. He suggested that the impacting particles must be less than a critical size. Conversely, Finnie²⁸ proposed a minimum particle size, below which the erosion process becomes ineffective. Tilly²⁹ observed the size distribution of abrasive both before and after testing, and found a change in particle size distribution suggesting particle breakup. Schmeltzer²⁶ found no change in particle distribution before and after impact testing. Nor did either author observe any microscopic evidence of particle breakup. Instead, both observed massive plastic flow, with abrasive particles embedded in the metal surface. These authors report evidence of melting around craters formed on the crystal surface.

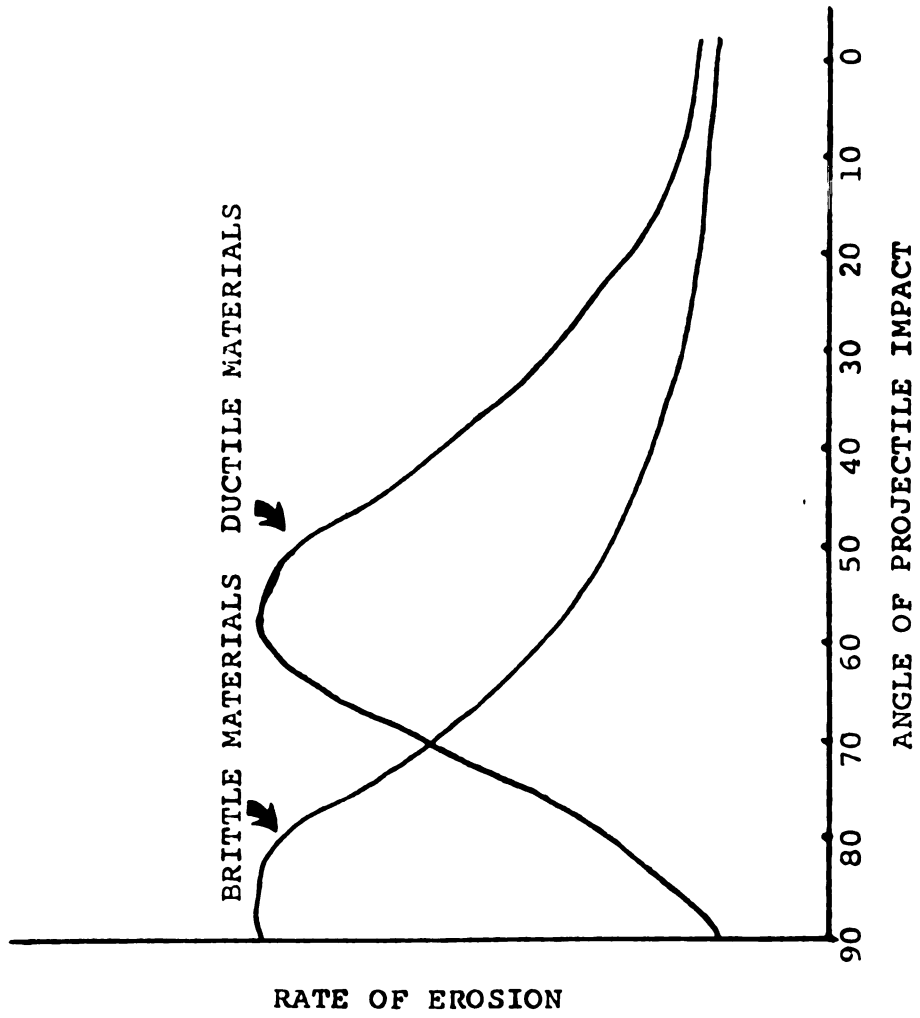
Wiederhorn and Roberts¹ in studying erosion of a castable refractory at temperatures from 25°C to 1500°C observed a transformation in the mode of erosion as a function of temperature. At 25°C , material loss occurred by brittle fracture of the refractory surface, and at 1000°C by shear deformation and fracture. At 25°C , the rate of erosion was greatest in normal impact where material loss takes place through

brittle failure. At 1000°C, however, the rate of erosion is greatest at impact angles between 0° and 30°, as the loss mechanism presumably changes from brittle failure to ductile flow. In other brittle materials, Hockey et al.²² have also found a dependence of the extent and the mode of erosion on the angle of impact. At low angles of impact (less than 15°) the extent of surface cracking is considerably reduced. Cracks produced by sharp particles were predominantly of the lateral-vent type,²² with median-vent crack formation largely suppressed. The mode of erosion changed distinctly from high to low angles of impact, with the particles removing material primarily by ploughing.

If plastic flow is the primary mechanism of erosion at low angles of impact, materials of the same hardness but of different fracture toughness should have the same erosion rate. Hockey et al.²² observed a change in the rate of erosion as a function of the angle of impact, at temperatures from 25°C to 1000°C, as did Wiederhorn and Roberts.¹ Hockey et al.²² attributed this change to increased plasticity at higher temperatures. The results of this investigation by Wiederhorn and Roberts¹ and that of Hockey et al.²² agree closely with the results of investigation by Sheldon.³¹ He found that ductile materials sustain the greatest erosion when the angle of blunt projectile approach was about 30°. In brittle materials, erosion wear was greatest at an angle of impact of 90° from the surface as illustrated by Figure 4. A semi-empirical formula for ductile materials that gives the volume of material removed by an abrasive particle of mass, m , is

$$W = \frac{k m V^2}{p} f(\alpha) , \quad (2)$$

Fig. 4. Rate of erosion versus angle of impact.



where W = the rate of erosion, (Kg/s),
 p = the dynamic flow pressure of the material, (Kg⁵/m²),
 V = the velocity of the particle, (m/s), and
 $f(\alpha)$ = a function of the angle of impact.

For ductile targets, this equation is independent of abrasive size.

Based in part on the Hertz expression for the contact of a sphere on an isotropic half-space, the erosion rate--which also depends on the projectile size and shape--is given by:

$$W = kr^a V^b \quad (3)$$

where W = the rate of erosion, (kg/s),
 k = the material characteristic parameter,
 a, b = shape parameters,
 V = the particle velocity, (m/s), and
 r = the particle diameter, (m).

Finnie³² combined Hertz's analysis with Weibull's statistical treatment of the effect of flaws. Brittle materials start to erode in a characteristically ductile manner if the erosive particles are sufficiently small, since the probability of a critical size flaw decreases as the particle size decreases. The stressed volume of the crystal is sufficiently small so that plastic flow can occur before fracture.

Most theories of erosion of brittle materials are based on Hertz's³³ analysis of the stresses generated when an isotropic elastic sphere is pressed quasi-statically against a flat, isotropic half-space.^{33,34}

In Greszczuk's³⁴ modification of Hertz's analysis, the force of impact (p), area of contact (a), surface pressure distribution (q), and duration of impact (t), may be calculated from the following expressions:

$$p = \frac{4\sqrt{R_p}}{3\pi(k_t + k_p)} \frac{5V^2}{4nn_1} \quad (4)$$

$$a = R_p^{0.5} V^{2/5} \left\{ \frac{15m_p m_t [E_p(1-\nu_t^2) + E_t(1-\nu_p^2)]}{16\sqrt{R_p} (m_p + m_t) E_p E_t} \right\}^{1/5} \quad (5)$$

$$q =$$

$$\frac{2 E_t E_p}{n\sqrt{R_p} [(1-\nu_t^2)E_p + (1-\nu_p^2)E_t]} \left\{ \frac{15[(1-\nu_t^2)E_p + (1-\nu_p^2)E_t] m_p m_t V^2}{16\sqrt{R_p} E_t E_p (m_t + m_p)} \right\}^{1/5} \left(1 - \left(\frac{r}{a}\right)^2\right)^{0.5} \quad (6)$$

$$t = \frac{2.94}{V} \left[\frac{9\pi^2 p^2 (k_t + k_p)^2}{16 R_p} \right]^{1/3} \quad (7)$$

where R_p = radius of the particle, (m),

E_p, E_t = modulus of elasticity for the particle and target,

ν_p, ν_t = Poisson's ratio of the particle and target,

$$k_t = \frac{1 - \nu_t^2}{\pi E_t} ,$$

$$k_p = \frac{1 - \nu_p^2}{\pi E_p} ,$$

$$n = \left[\frac{4}{3\pi(k_t + k_p)} \right] \sqrt{R_p} ,$$

$$n_1 = \frac{1}{m_t} + \frac{1}{m_p} , \text{ and}$$

V = velocity of the projectile (m/s) .

The maximum tensile stress (σ_t), compressive stress (σ_c), and shear stress (σ_s), in the target can be determined from Hertz's analysis by

$$\sigma_t = - \left(\frac{1-2\nu_t}{3} \right) q , \quad (8)$$

$$\sigma_c = q , \quad \text{and} \quad (9)$$

$$\sigma_s = \left[\frac{1-2\nu_t}{4} + \frac{\sqrt{2(1+\nu_t)^2}}{9} \right] q , \quad (10)$$

where ν_t = Poisson's ratio of the target, and

q = surface pressure distribution.

Physical damage arises from a characteristic Hertzian cone crack.³⁶

This crack is proposed to develop from a random flaw situated in the surficial region of high stress near the circle of contact. The crack, which has the shape of the frustum of the cone, penetrates the solid a distance determined by the magnitude of the load. Two or more cracks must intersect for material loss to occur. Such loss depends on the distribution of flaws in the surface as well as on the test conditions as illustrated by Figure 5. Greszcuk's analysis has been shown to correlate well with experimental observations in the erosion of glass.^{37,38} In a preliminary study, Lawn and Wilshaw³⁶ observed that impact damage observed under fully plastic contact conditions is identical in form to that obtained under quasi-static conditions. This damage consists of radial, lateral, and median cracks outside a central plastic impression. The appearance of damage suggests that Lawn's³⁵⁻⁴⁴ theories of deformation under sharp and blunt indenters may be applicable to the erosion behavior of brittle materials. For blunt indenters in perfectly elastic contact, crack initiation is controlled

The maximum tensile stress (σ_t), compressive stress (σ_c), and shear stress (σ_s), in the target can be determined from Hertz's analysis by

$$\sigma_t = - \left(\frac{1-2\nu_t}{3} \right) q , \quad (8)$$

$$\sigma_c = q , \quad \text{and} \quad (9)$$

$$\sigma_s = \left[\frac{1-2\nu_t}{4} + \frac{\sqrt{2}(1+\nu_t)^2}{9} \right] q , \quad (10)$$

where ν_t = Poisson's ratio of the target, and

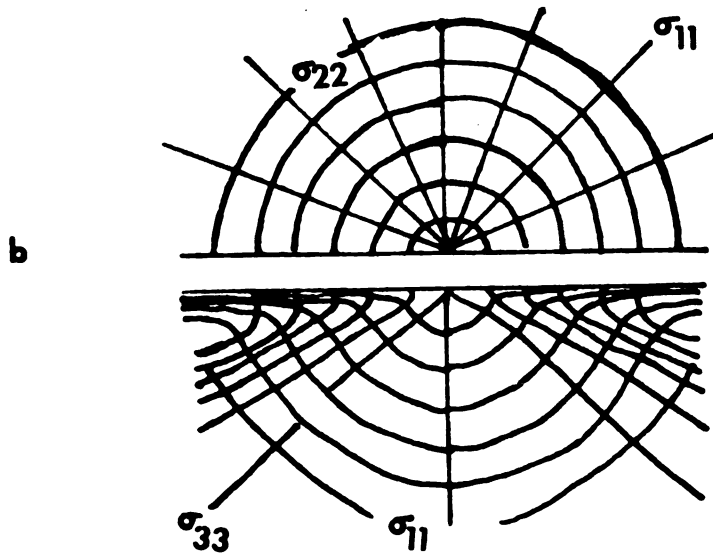
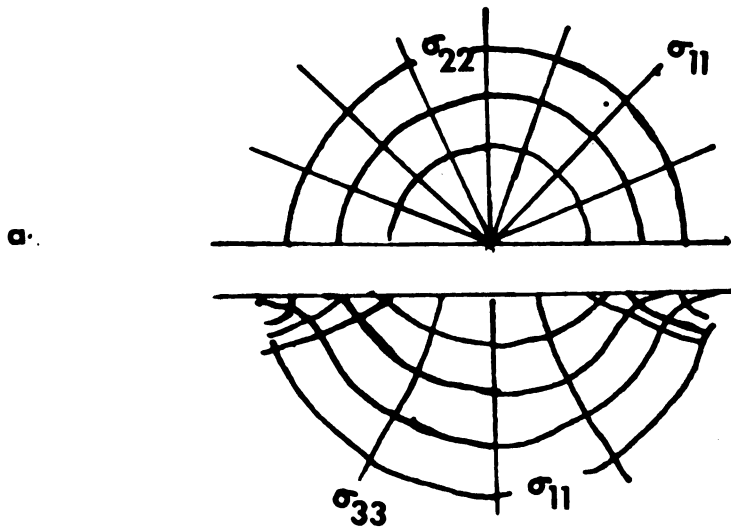
q = surface pressure distribution.

Physical damage arises from a characteristic Hertzian cone crack.³⁶

This crack is proposed to develop from a random flaw situated in the surficial region of high stress near the circle of contact. The crack, which has the shape of the frustum of the cone, penetrates the solid a distance determined by the magnitude of the load. Two or more cracks must intersect for material loss to occur. Such loss depends on the distribution of flaws in the surface as well as on the test conditions as illustrated by Figure 5. Greszcuk's analysis has been shown to correlate well with experimental observations in the erosion of glass.^{37,38} In a preliminary study, Lawn and Wilshaw³⁶ observed that impact damage observed under fully plastic contact conditions is identical in form to that obtained under quasi-static conditions. This damage consists of radial, lateral, and median cracks outside a central plastic impression. The appearance of damage suggests that Lawn's³⁵⁻⁴⁴ theories of deformation under sharp and blunt indenters may be applicable to the erosion behavior of brittle materials. For blunt indenters in perfectly elastic contact, crack initiation is controlled

Fig. 5. Impact stress field for:

- a. a Hertzian stress field (blunt projectile impact);**
- b. a Boussinesq stress field (sharp projectile impact).**



by pre-existing flaws at the specimen surface. For sharp indenters in partially plastic contact, the starting flaws do not appear until the indentation itself occurs. Deformation-induced flaws tend to nucleate at points of intense stress concentration ahead of zones of inelastically deformed material. For sharp indenters, a deformation-induced flaw develops into a small crack on a plane of symmetry containing the contact axis. An increase in loading causes this median vent to grow. Upon unloading, the median crack begins to close and lateral vents develop. For blunt indenters, fracture begins from a pre-existing flaw and grows by running horizontally around the contact in an effectively uniform σ_{11} field, closely following the circular σ_{22} stress trajectories. Vertical propagation of the surface ring crack occurs less readily because of the rapidly diminishing field beneath the free surface but proceeds along the σ_{33} trajectories as illustrated by Figure 5, where σ_{11} , σ_{22} , and σ_{33} are the principal stresses. According to Lawn and Wilshaw,³⁶ there is some compromise between the tendency for cracks in single crystals to follow stress trajectories and cleavage planes.

The Boussinesq field has been chosen by Lawn and Wilshaw³⁶ to describe damage produced by sharp indenters. The Boussinesq field describes an isotropic, linear elastic half-space subjected to a normal point load, P . The magnitude of the stresses is proportional to the applied load and to the inverse square of the radial distance from the point of contact, times an independent angular function of Poisson's ratio, $v_{ij}(\varphi)$, or

$$\sigma_{ij} = \left(\frac{P}{\pi R^2} \right) [v_{ij}(\varphi)] \quad ,$$

where R = the radius of the indenter, and

$[\nu_{ij}(\varphi)]$ = an angular function of Poisson's ratio.

Adler⁴⁵ studied the impact-erosion behavior of silicate glass impacted by blunt projectiles (glass beads). He found that the major mode of damage was through the formation of a Hertzian cone fracture. Material loss occurred where the lateral fractures intersected. Also, he found that there was a relatively good correlation between the observed diameter of the contact area and the contact area calculated through Hertz's analysis.

1.3 Objectives

The objective of this work is to determine the role of microscopic deformation on macroscopic erosion damage. The effects of particle velocity, shape, and size will be considered as they affect erosion in brittle and semi-brittle materials. In the erosion of brittle materials, some authors have proposed the existence of a critical velocity below which no damage is observed. One objective of this study is to determine the relationship between material properties and the critical velocity required to produce erosion damage. Another objective is to determine if the theories of Lawn for blunt and sharp indenters can be applied to the erosion of brittle ceramic materials. Ultimately, an objective of this study is to understand the basic mechanisms of deformation of brittle and semi-brittle crystals under dynamic loading.

2. EXPERIMENTAL PROCEDURE

As targets, single crystals of a range of hardness were chosen. High-purity LiF, NaCl, KCl, and CaF₂ single crystals were commercially obtained. These materials decrease in hardness in the order CaF₂ > LiF > NaCl > KCl, where the hardness on the Mohr scale for CaF₂ is 4.5, LiF is 3, NaCl is 2.5, and KCl is 2. Special care was taken to minimize handling of the crystals.

2.1 Sample Preparation

Samples were cut or cleaved from bulk crystals that had been stored in a desiccator in order to minimize degradation from moisture. NaCl and KCl are especially hygroscopic and deteriorate rapidly under humid conditions.

LiF, NaCl, and KCl samples to be eroded on the {100} were cleaved into parallelepiped from bulk crystals. The dimensions of the samples were approximately 10 mm x 5 mm x 3 mm. CaF₂ samples to be eroded on the {111} were also cleaved from bulk crystals and had a wedge-shaped surface approximately 50 mm² in area exposed to erosion.

LiF, NaCl, and KCl samples to be eroded on the {110} and {111} faces were cut from bulk crystals with a Buehler diamond saw. The crystals were mechanically polished with 600- grit SiC, and 5 and 0.5 micron grit alumina. After polishing, the crystals were chemically polished by glass-distilled water. Chemical polishing removed the disturbed layer that resulted from mechanical polishing.

2.2 Impact-Erosion Experiments

2.2.1 Projectiles

In this study, the crystals were eroded by three types of projectiles. The glass beads (blunt projectiles), shown in Figure 6a, had a bimodal distribution in diameter. Ninety-five percent of the beads had an average diameter of 0.25 mm with a standard deviation of 0.035 mm. The remaining beads had an average diameter of 0.05 mm with a standard deviation of 0.01 mm.

Standard Ottawa quartz sand (blunt projectiles), shown in Figure 6b, is from a glacial terrain and is highly weathered and rounded. These grains had an average diameter of 0.50 mm with a standard deviation of 0.02 mm. Quartz sand and glass have a hardness of approximately 7 on the Mohr scale.

Silicon carbide particles (sharp projectiles), shown in Figure 6c, had sharp points and edges with relatively flat sides, with an average diameter of 0.175 mm with a standard deviation of about 0.03 mm. Silicon carbide particles have a hardness of approximately 9.5 on the Mohr scale.

2.2.2 Low-Temperature Testing

Samples were tested at 25^oC in an air-jet abrasive device as shown in Figure 7. Dry nitrogen gas was the carrier medium accelerating the abrasive particles to the desired velocity as they passed along a 6 cm-long fused silica nozzle. This was monitored by stopping the flow of nitrogen gas and reading the tank gas pressure.

Comparisons of particle velocity and gas-flow velocities in several systems have shown large differences, attributed mainly to

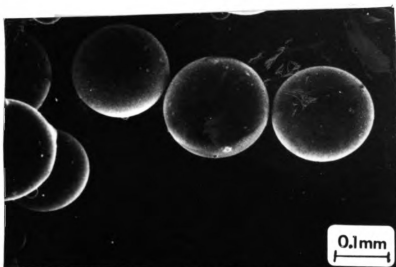
Fig. 6. Particles used as projectiles for impact damage.

a. Glass beads.

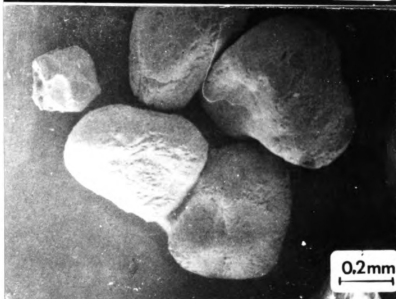
b. Quartz sand.

c. SiC.

a



b

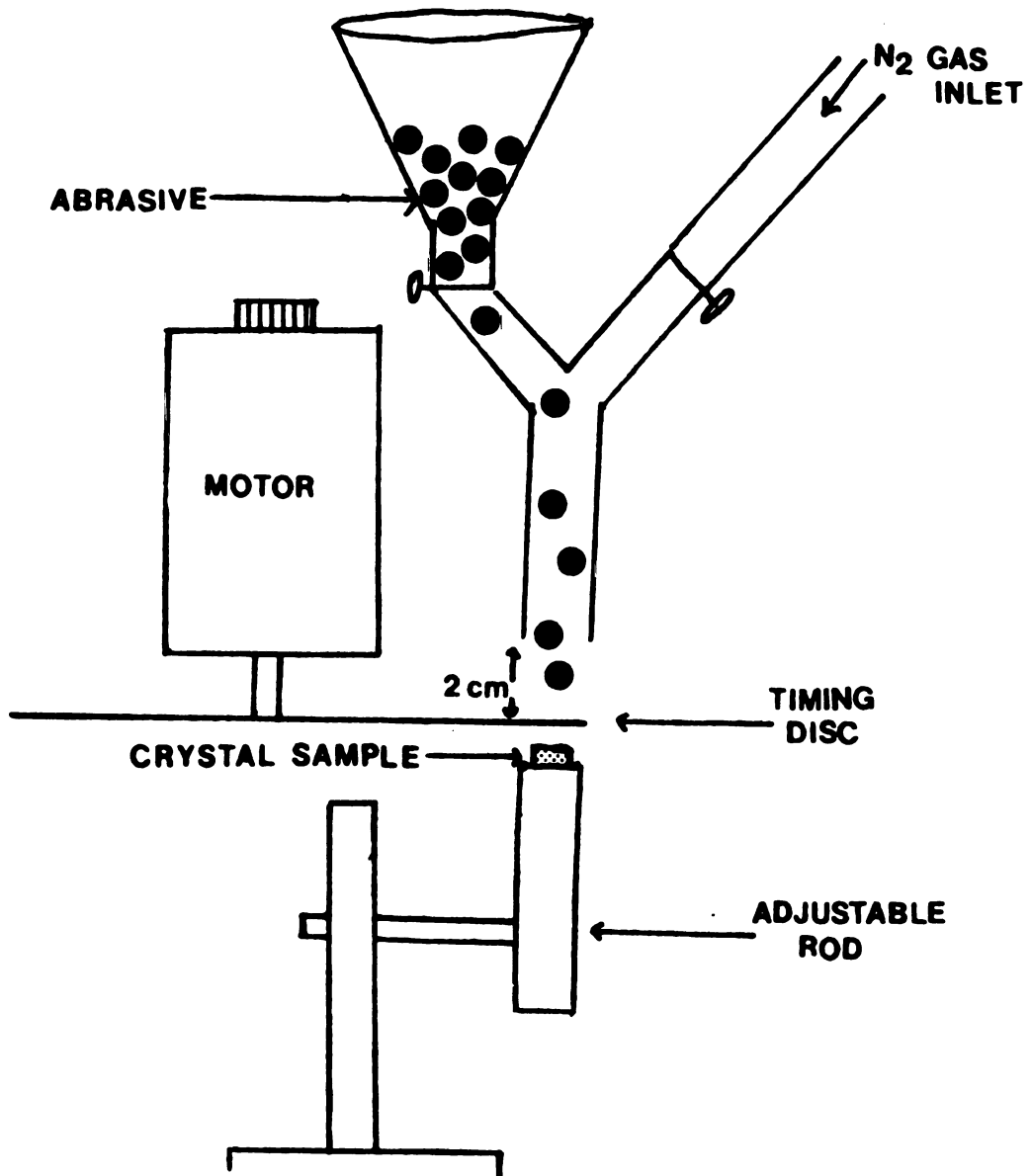


c



**Fig. 7. Room-temperature test apparatus with jet-air
abrasive device, sample holder and timing disc.**

20(a)



turbulence. Therefore, particle velocity was determined by a method developed by Ruff and Ives.⁴⁶ In this method, two discs are rotated on a common axis as shown in Figure 8. When the abrasive particles pass through the slit and hit the lower disc, they are displaced by an angle determined by the partial velocity, spacing of the discs, and the angular velocity of the discs.

The average particle velocity can be determined by:

$$V = 2\pi t \omega L/s$$

where s = the linear displacement of the abrasion marks, (in cm),

L = the separation of the discs, (in cm),

ω = the angular velocity of the discs, (in rad/sec), and

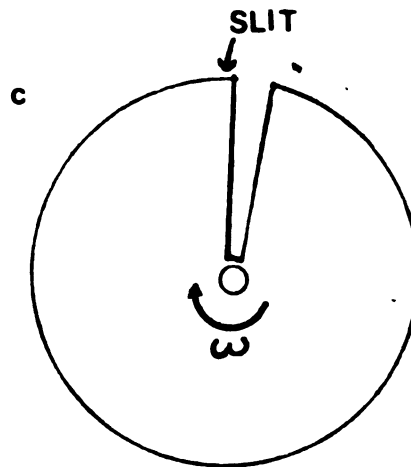
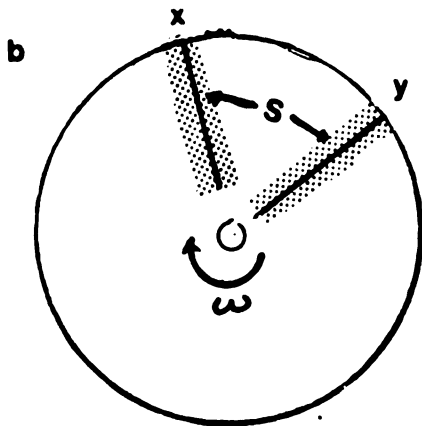
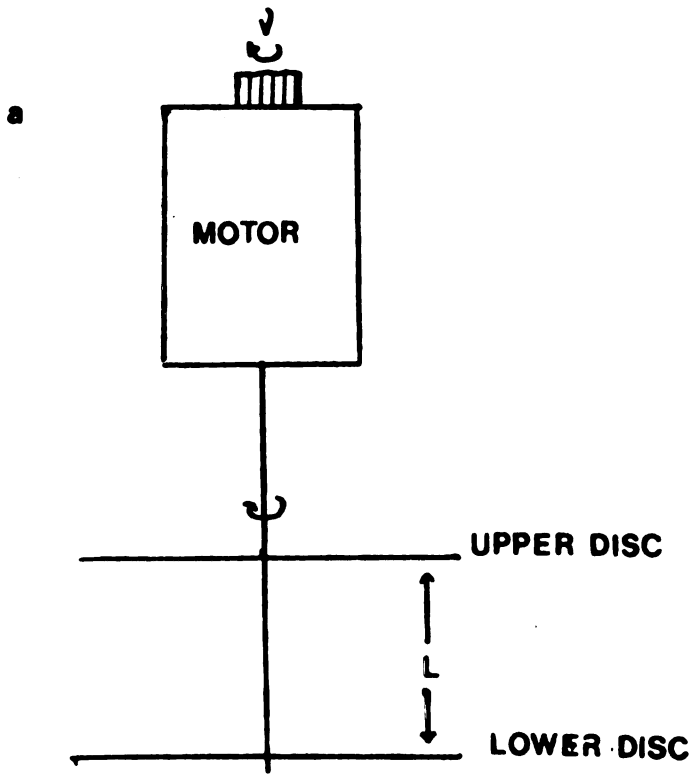
t = the time (in sec).

At each gas pressure, variation in the rate of flow was tested by timing the flow of a given weight of abrasive at a set gas pressure. Variations were found to be negligible. The particle velocity was measured periodically before testing to determine changes in velocity due to wear of the nozzle.

Exposure time was controlled by a rotating disc shown in Figure 8. An aluminum disc with a 20° wedge was rotated at a constant angular velocity. Time of exposure was controlled by controlling the number of rotations of the disc. The angular velocity of the disc was chosen low enough that the number of revolutions could be manually controlled. The samples were held on an aluminum rod at a distance of 2 cm below the exit end of the nozzle to allow clearance for the timing disc to pass between the nozzle and the sample. The angle of inclination of

Fig. 8. Experimental set-up for velocity measurement at low temperatures.

- a. Schematic.**
- b. Lower disc (x=stationary mark, y=dynamic mark)**
- c. Upper disc with slit cut out.**



the sample holder was adjustable to allow the samples to be eroded at angles of up to 60° from an axis normal to the surface of the crystal.

2.2.3 High-Temperature Testing

Samples of LiF were eroded at 200°C and 400°C to see if temperature affected the mode of erosion. Modifications in the test equipment as shown in Figure 9 were necessary for the high-temperature work.

An air-jet abrasive device eroded the samples. To avoid thermal stresses in the sample, the carrier gas, dry nitrogen, was preheated by passing it through a copper tube. The temperature was measured with a thermocouple placed near the sample.

The exposure time was determined by weighing the amount of abrasive. For a constant gas velocity, the exposure time could be calculated by determining the rate of abrasive flow for a given velocity and weight of abrasive.

2.3 Microscopic Analysis

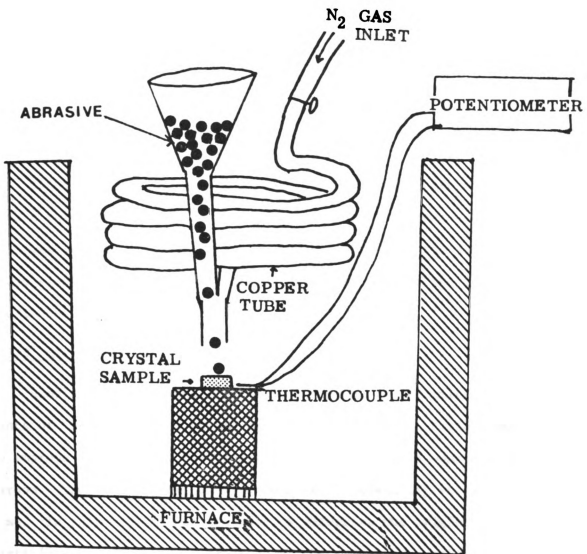
After testing, samples were etched and examined by optical and scanning electron microscopy. The usefulness of optical microscopy was severely limited by the depth of focus. Optical microscopy could resolve damage from only the earliest stages of erosion.

2.3.1 Etchants

After testing, LiF and CaF_2 samples were etched to reveal slip bands. For lithium fluoride the etchant was a dilute solution of ferric chloride in distilled water. In contrast, for calcium fluoride the etchant was a solution of 50 ml distilled water, 20 ml glacial

Fig. 9. High-temperature apparatus with jet-air abrasive device, sample holder, and furnace.

24(a)



acetic acid, 2 drops of HCl, and 16 drops of nitric acid at 100°C. The time required to etch the crystals varied somewhat from crystal to crystal.

2.3.2 Scanning Electron Microscopy

Selected samples were examined by a ISI Super II scanning electron microscope. Details of the damage within the circle of contact could be observed with a scanning electron microscope because of the enhanced depth of focus. These details could not be resolved by optical microscopy.

Since the samples were electrical nonconductors, they were coated with a thin (about 100 Å) layer of a gold alloy in an evacuated chamber. This was done to eliminate charging on the surface of the sample. These samples were tilted in the microscope to improve the contrast of the image.

2.3.3 Microprobe Analysis

Samples were examined by an ARL microprobe to determine if fragments of the projectiles became embedded in the sample during impact. To improve electrical conductivity, these samples were coated with carbon. The samples were examined at 50KV accelerating voltage and 2 ma. In this way, it was possible to determine the origin of the particle--whether it was a fragment of the sample, a fragment of the projectile, or a foreign object. Point counts were taken across the circle of contact by moving the sample under a stationary beam.

By this method, distortion of the count rate that would occur if the beam moved and the sample remained stationary was eliminated.

Background counts were taken on both sides of the X-ray peaks to determine the mean background counts to be subtracted from the total counts. At the beginning and at the end of each session, point counts were taken on standards to determine if drift occurred during the analysis.

3. RESULTS AND DISCUSSION

Damage produced during erosion is highly dependent on the nature of loading. The applied stress field can, in part, be estimated from the shape of the particle. A blunt particle would be expected to produce a Hertzian stress field, a sharp particle a Boussinesq stress field.

3.1 Single Impact Damage Produced by Blunt Projectiles

The Hertzian stress field has often been proposed as a starting point for analysis of impact-erosion damage.^{37,38,40,45} Within the field, according to Lawn and Wilshaw,³⁶ fracture is initiated from pre-existing or induced flaws in the material. These flaws, which are sub-microscopic, arise during the complex mechanical, thermal and chemical history of the material. Whether a flaw becomes critical for fracture propagation depends on its size, position, and orientation within the tensile field. Upon attaining a "critical configuration," a dominant flaw develops into a well-defined, propagating crack. Lawn and Wilshaw³⁶ have stated that in crystals with strong cleavage tendencies there is some compromise between the tendencies for cracks to follow stress trajectories and to follow cleavage planes.

3.1.1 Low-Temperature Slip and Crack Nucleation at Normal Impact on the Cleavage Plane.

Single-particle impact damage closely resembles quasi-static blunt-indenter damage.³⁶ Above the critical impact velocity the damage

is characterized by a contact zone from which a set of lateral fractures spreads out.^{36,37}

The critical velocity is defined as the velocity of impact at which lateral fractures appear in ceramic materials. This velocity is much lower in CaF_2 than in the more ductile materials LiF, NaCl and KCl. In CaF_2 lateral fractures develop at velocities of less than 2 m/s, as shown in Figure 10. As the ductility of the material increases, the critical velocity increases. In LiF, for example, it is greater than 5 m/s. At impact velocities below critical, only slip is evident at the area of impact.

The damage is characterized by a rosette pattern of dislocations about the point of impact. On the $\{100\}$ surface in LiF, damage is revealed by etch pits formed at dislocations along the $\{101\}$, $\{011\}$ and $\{110\}$, as shown in Figure 11 (the $\{101\}$, $\{011\}$ and $\{110\}$ planes are shown in Figure 12). This rosette pattern has also been observed in NaCl,⁴⁷ KCl,⁴⁸ and MgO.⁴⁸⁻⁵⁰ Etch pits are formed at screw-dislocation lines along the $\{110\}$, and also at edge-dislocation lines along the $\{101\}$ and $\{011\}$. These planes are those of the well-known slip systems of NaCl-structure crystals at room temperature, namely $\{110\}\langle 1\bar{1}0\rangle$.

In CaF_2 , as in LiF, extensive slip occurs at low-impact velocities. In CaF_2 , however, slip occurs in the $\{100\}\langle 011\rangle$ system.^{50,51} A cluster of triangular-shaped etch pits can be observed about the point of impact. These pits are arranged in a hexagonal pattern, reflecting the symmetry of the crystal as can be seen in Figure 10.

The contact zone for a blunt indenter is characterized by massive plastic flow. Microfracture within the region of contact is extensive,

Fig. 10. A scanning electron micrograph of CaF_2 eroded by 0.25 mm glass beads impacting the $\{11\bar{1}\}$ at a velocity of 2 m/s.

29(a)

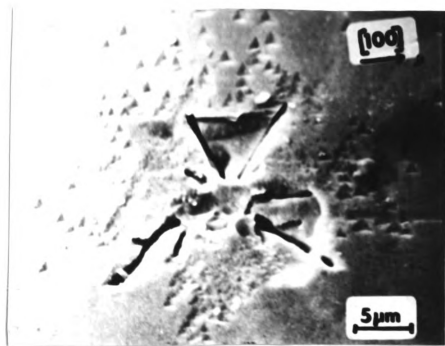


Fig. 11. A scanning electron micrograph of LiF eroded by 0.25 mm glass beads impacting the {001} at a velocity of 10 m/s (etched).

30(a)

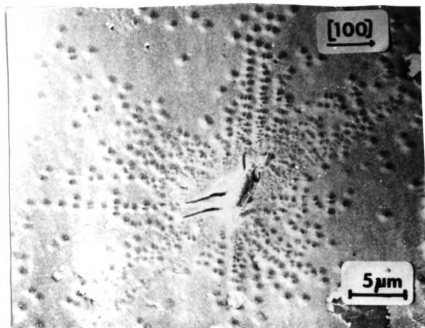
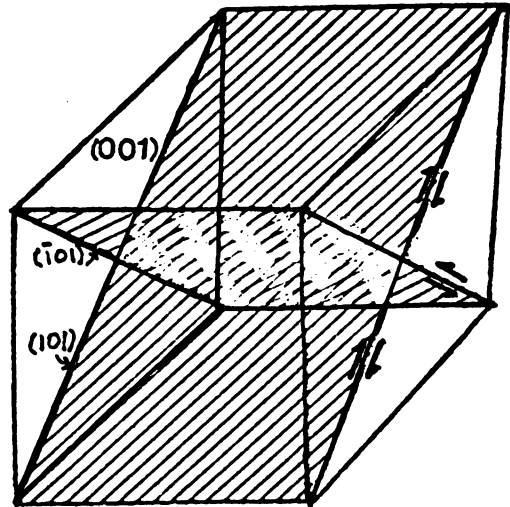
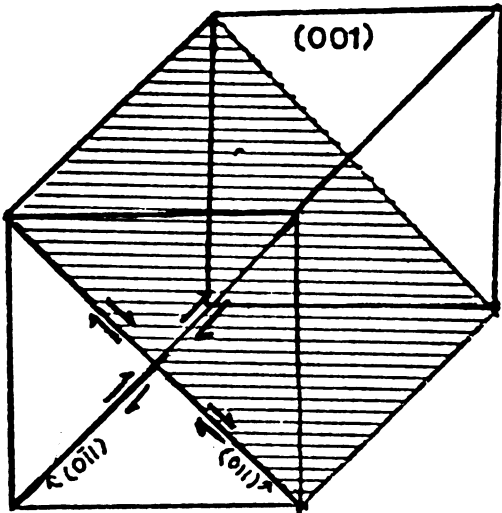
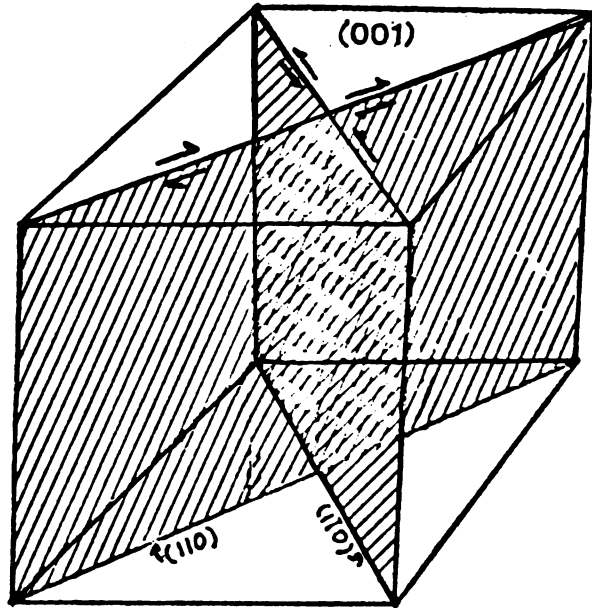


Fig. 12. Orientation of the $\{011\}$, $\{101\}$, and $\{110\}$ planes.

31(a)



as shown in Figure 13a. These fractures, which appear to be curved, depart from specific crystallographic directions, as seen in Figure 13b. This appearance may be due to reorientation of crystal segments, as suggested in Figure 14. During impact, material in the contact zone is rapidly work-hardened, as illustrated in Figure 14a. This material cleaves along preferred crystallographic planes to produce numerous microcrystals as illustrated in Figure 14b. As the deformation continues, the material flows outwardly to accommodate the rapid displacement. During flow, the microcrystals become reoriented and thus appear to have curved boundaries as shown in Figure 14c.

In the case of the ductile crystals KCl and NaCl, plastic flow is extensive. At impact velocities greater than 25 m/s, embedding of whole projectiles can occur, as shown in Figure 15. In LiF (intermediate ductility), embedding of whole projectiles is not observed but at impact velocities greater than 30 m/s, some fragmentation and embedding of projectile fragments has been observed by microprobe examination. In the brittle CaF_2 , embedding of neither projectiles nor fragments is observed.

Unlike more ductile materials, CaF_2 does not exhibit extensive plastic deformation in the contact zone. Extensive microfracturing, however, does occur there, as seen in Figure 16. Often, a complete ring fracture is developed at the zone perimeter, as can be seen in Figure 17. Lateral fractures are developed outside the contact zone. In NaCl-structure crystals, which are less brittle, four lateral fractures result during normal impact as illustrated in Figure 18. These fractures originate outside the contact zone. Although numerous microfractures occur just within the circle of contact, usually only four

Fig. 13. A scanning electron micrograph of LiF eroded by 0.25 mm glass beads impacting the {001} at a velocity of 45 m/s (etched).

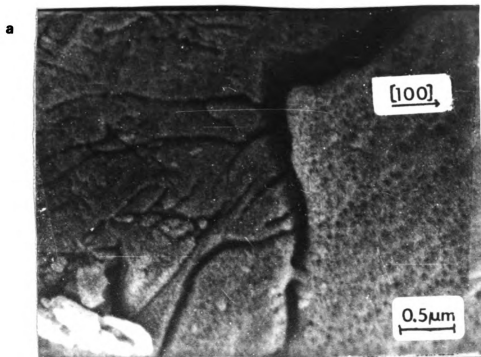


Fig. 14. Formation and reorientation of chips during impact.

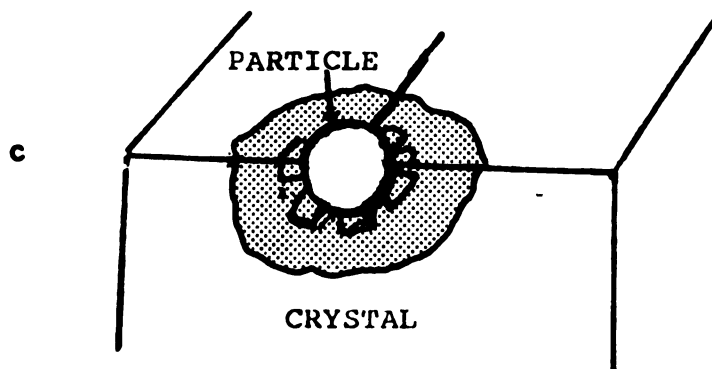
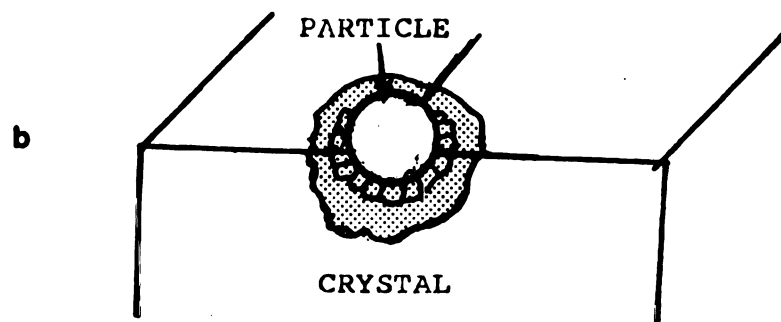
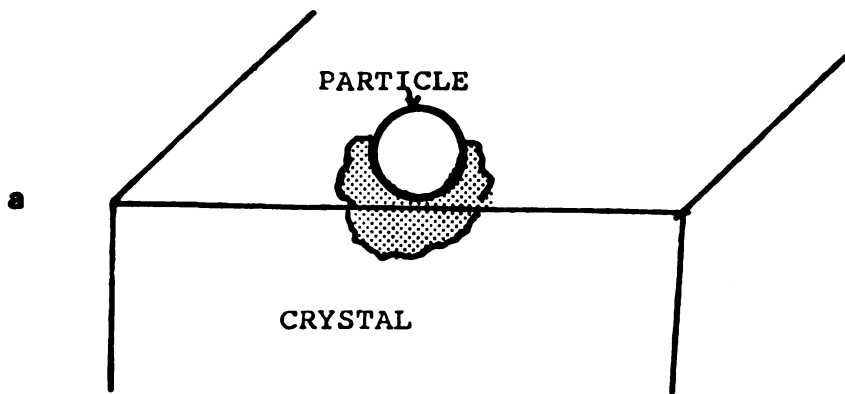


Fig. 15. A scanning electron micrograph of KCl eroded by 0.25 mm glass beads impacting the {001} at a velocity of 25 m/s.

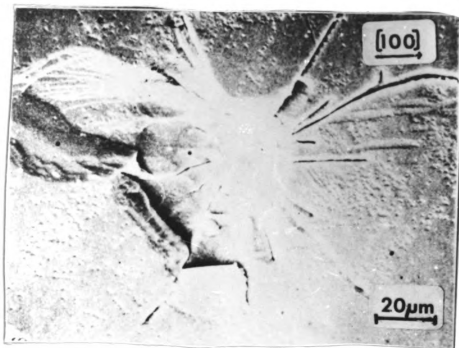
35 (a)



- Fig. 16. A scanning electron micrograph of CaF_2 eroded by 0.25 mm glass beads impacting the $^{2}\{111\}$:
- a. at a velocity of 45 m/s;
 - b. at a velocity of 30 m/s (etched).

36(a)

a



b

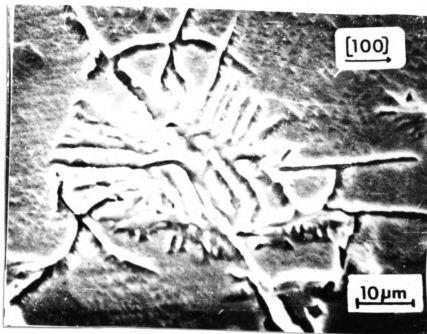


Fig. 17. A scanning electron micrograph of CaF_2 eroded by 0.25 mm glass beads impacting the $\{111\}$ at a velocity of 30 m/s.

a. Single impact.

b. Double impact.

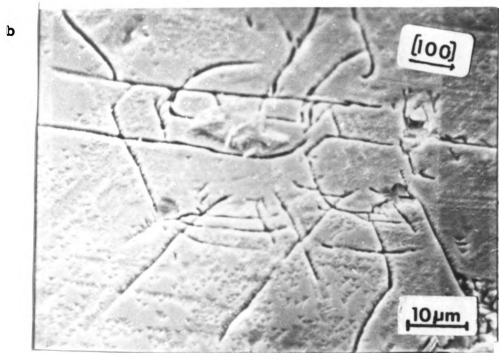
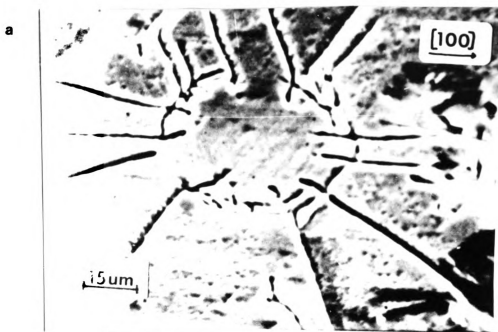
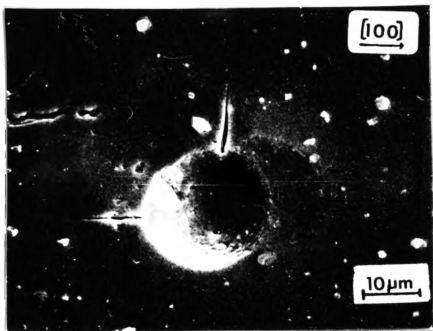


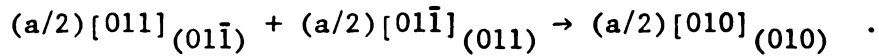
Fig. 18. A scanning electron micrograph of NaCl eroded by 0.25 mm glass beads impacting the {001} at a velocity of 25 m/s.

38(a)

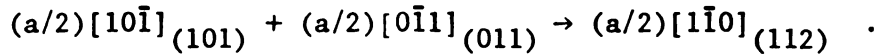


major lateral fractures are developed outside it. A ring fracture is only partially developed at the edge of the circle. This fracture contrasts with the prominent ring fractures observed in silicate glass by Adler⁴⁵ as shown in Figure 19.

In NaCl and KCl, fractures are developed along the $\langle 100 \rangle$. These fractures are developed as the result of slip on the $\{110\}\langle \bar{1}\bar{1}0 \rangle$ system. In NaCl and KCl, cracks are formed by the reaction:



In LiF, lateral fractures are formed through the reaction:



The reacted $(a/2)[1\bar{1}0]$ edge dislocation has a line vector parallel to the $(a/3^{\frac{1}{2}})[11\bar{1}]$.⁴⁹ This dislocation is contained in the (112), and is sessile for NaCl-structure crystals. Once the dislocations are reacted, they prevent additional displacement of the crystal along the $[00\bar{1}]$. This downward displacement is necessary to maintain negligible volume change for the continuing impact process.⁴⁹ Cleavage along the $[1\bar{1}0]$ allows for upward displacement of the crystal.⁴⁹ The reacted sessile dislocations prevent the backward flow of dislocations and the relaxation of the unloaded material. Multiple impact causes the accumulation of work hardening in the material.

Similar fracture patterns occur on the (010). In LiF, fracture occurs along the (011) and $(0\bar{1}1)$, as illustrated by Figure 20. Superficially, this fracture pattern mimics a classical Hertzian cone fracture. In contrast, in NaCl and KCl, fracture occurs on the (010).

Fig. 19. A scanning electron micrograph of LiF eroded by 0.50 mm blunt projectiles impacting the {001} at a velocity of 45 m/s (etched).

40 (a)

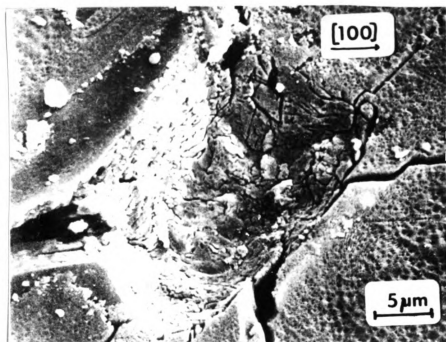
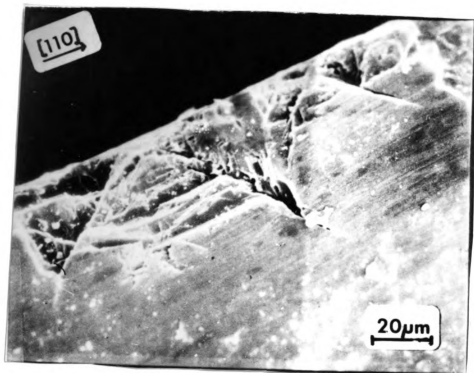


Fig. 20. A scanning electron micrograph of LiF eroded by 0.25 mm glass beads impacting the {001} at a velocity of 45 m/s. The plane of observation is the {010}.

41(a)



At very high impact velocities, {101} and {011} cracking is occasionally observed in LiF, as shown in Figure 21. With particle-embedding in NaCl as shown in Figure 18, lateral fracture is observed along the {101}, {011} and {110}.

In CaF₂, three types of fractures have been observed.⁵⁰ The fracture occurs on the {100}, {110}, and {111}. The dislocation reaction involved in the formation of {100} fractures can be represented by:

$$\frac{1}{2} a [0\bar{1}1] + \frac{1}{2} a [0\bar{1}\bar{1}] = a [0\bar{1}0] .$$

This reaction resembles the mechanism suggested by Cottrell⁵² for the formation of cleavage cracks on the {100} in body-centered cubic crystals, even though in CaF₂ crystals the elastic energy does not change in the reaction. These {100} cracks propagate readily along the surface, but encounter difficulty in propagating into the interior of the crystal.⁵⁰ Although the {111} is the typical cleavage plane, a crack formed on a {111} face must pass through dislocation pile-ups at {100} intersections. These regions are regions of high stress that oppose the tensile stress aiding the propagation of the crack.⁵⁰

The {110} cracks also propagate more readily along the surface than through the crystal interior. These fractures are formed by the reaction:

$$\frac{1}{2} a [0\bar{1}1] + \frac{1}{2} a [10\bar{1}] = \frac{1}{2} a [1\bar{1}0] .$$

This reaction is favored in terms of the elastic energy released, although {100} fractures are more common. The formation of chips between the lateral fractures of single impacts in CaF₂, as shown in

Fig. 21. A scanning electron micrograph of LiF eroded by 0.50 mm blunt projectiles impacting the {001} at a velocity of 35 m/s (etched).

43(a)

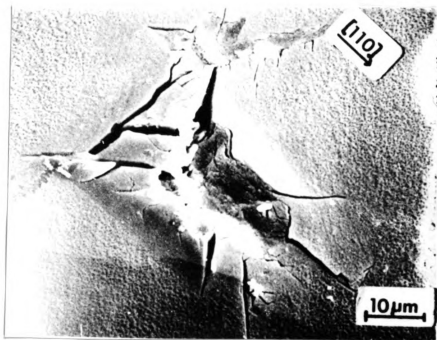


Figure 22, is the result of the difficulty of $\{100\}$ and $\{110\}$ fractures in propagating through the interior of the crystal. These chips are characteristically much shallower than the length of the fracture. The size of the chip as well as the length of the lateral fractures increases proportionally with increasing velocity, as shown in Figure 22. The surface of the chip appears to be the result of a conchoidal fracture, similar to that in glass. This type of fracture has also been observed by Phillips⁵² in cleaved and annealed CaF_2 single crystals, and by Evans in ZnS .³⁹ The high stress field around the zone of contact, and the difficulty of $\{100\}$ and $\{110\}$ fractures in propagating into the interior of the crystal, lead to the formation of conchoidal fractures.

3.1.2 Normal Impact Erosion at Elevated Temperatures in LiF on the Cleavage Plane

With increasing temperature, changes occur in the mode of erosion in LiF. At room temperature, impact damage is characterized by a contact zone and four equidimensional mutually perpendicular lateral fractures. Severe plastic deformation and intense microfracturing occur within the contact zone.

At room temperature, the slip system in LiF is $\{110\}\langle 1\bar{1}0\rangle$. At higher temperature (200°C and 400°C), the $\{100\}\langle 01\bar{1}\rangle$ system becomes active, and the change in volume produced by impact can be accommodated by slip. The zone of contact takes on a faceted appearance at 200°C , as shown in Figure 23. Microfracturing, prominent at lower temperature, is absent at higher temperature, as shown in Figure 24. Lateral fractures, however, are still a prominent feature at 200°C . At an angle of impact of 30° from normal, the lateral fractures are displaced

Fig. 22. A scanning electron micrograph of CaF_2 eroded by 0.25 mm glass beads impacting the $^{2}\{111\}$ at a velocity of 15 m/s (etched).

45(a)

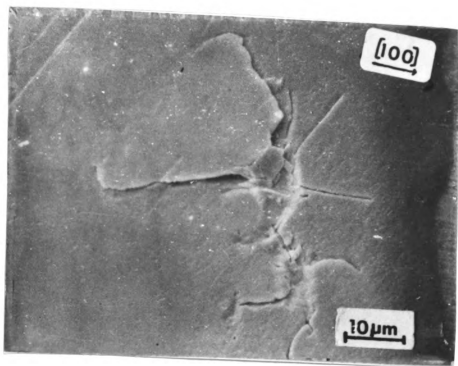


Fig. 23. A scanning electron micrograph of LiF eroded at 200°C by 0.50 mm blunt projectiles impacting the {001}:

- a. at an angle 90° from the crystal surface at a velocity of 45 m/s;
- b. at an angle 60° from the crystal surface at a velocity of 45 m/s (etched).

46(a)

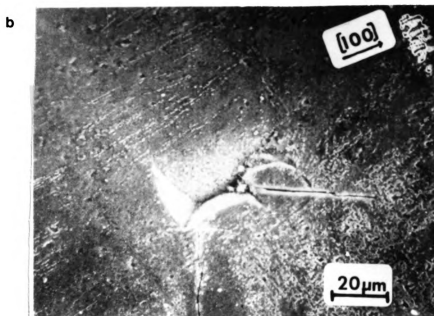
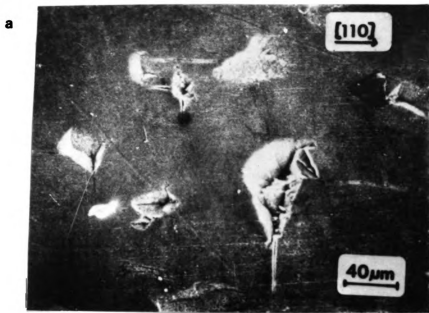
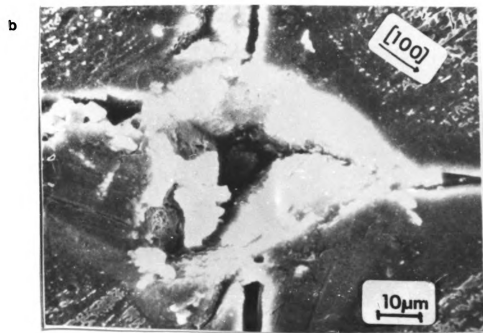
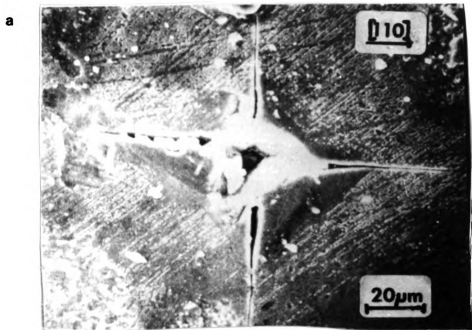


Fig. 24. A scanning electron micrograph of LiF eroded at 200°C by 0.50 mm blunt projectiles impacting the {001} at a velocity of 45 m/s (etched) ("b" is part of "a").

47(a)



about the zone of contact. Only two lateral fractures are present on one side of the faceted zone of contact, as shown in Figure 23b.

At 400°C, lateral fractures usually disappear, as shown in Figure 25a. No microfracturing occurs within the zone of contact, as shown in Figure 25b. Slip on the $\{100\}\langle 01\bar{1}\rangle$ and $\{110\}\langle 1\bar{1}0\rangle$ gives the zone of contact a faceted appearance.

An overall increase in plasticity with increasing temperature leads to a decrease in brittle failure during impact in LiF. The major change in the mode of erosion damage is the disappearance of microfracturing within the zone of contact. Instead, the zone of contact has a faceted appearance as the result of slip that accommodates the change in volume at the point of contact. Similar damage has been observed in quasi-statically produced indentations in MgO⁵⁰ at 550°C, where hexagonal, faceted indentations are likewise produced.

3.1.3 Slip and Crack Nucleation in NaCl-Structure Crystals on the $\{110\}$ and $\{111\}$ Planes at Normal Impact

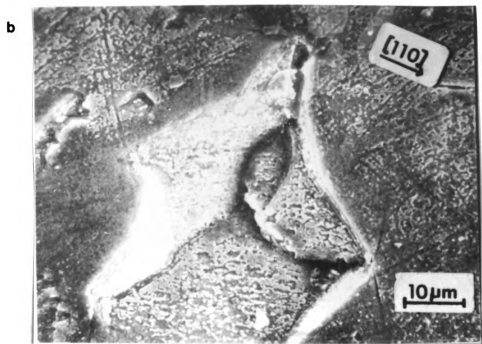
The mode of damage as the result of single normal impact with blunt projectiles is highly dependent on the existence of active slip systems. Whether a slip system will be active is, in part, dependent upon the orientation of the crystal axes relative to the direction of impact.

NaCl, KCl, and LiF samples were eroded at normal impact on the $\{110\}$ and $\{111\}$ faces in order to determine the effect of axis orientation on the mode of impact damage.

Samples eroded on the $\{110\}$ and $\{111\}$ show much less brittle failure than samples eroded on the $\{001\}$ as described earlier. The

Fig. 25. A scanning electron micrograph of LiF eroded at 400°C by 0.50 mm blunt projectiles impacting the {001}:

- a. at a velocity of 45 m/s;
- b. at a velocity of 60 m/s (etched).



major lateral fractures prominent in $\{001\}$ impact damage are absent in erosion on the $\{110\}$ and $\{111\}$. Microfracture within the zone of contact is absent even in LiF (intermediate) as shown in Figure 26a.

Many similarities exist between impact damage on the $\{110\}$ and $\{111\}$ in NaCl-structure crystals; for example, in the faceted indentations as shown in Figures 26-29. Damage on the $\{110\}$ and $\{111\}$ in KCl and NaCl (ductile materials) as shown in Figures 28a, 29a and 29b is almost identical to damage in LiF (intermediate) as shown in Figure 28a.

Single-impact deformation in NaCl-structure crystals can be accounted for by slip on the $\{110\}$, $\{011\}$, and $\{101\}$ planes as shown in Figure 30. In impact damage on the $\{111\}$ and $\{110\}$, there is a $\{110\}$ plane perpendicular to the surface of the crystal. Unlike the case of impact on the $\{100\}$, the direction of slip on the $\{110\}$ for impact on the $\{110\}$ and the $\{111\}$ allows for a downward displacement of the volume of the crystal to accommodate the displacement produced by the projectile. The direction of slip on the $\{110\}$ for impact on the $\{100\}$, in contrast, is perpendicular to the direction of displacement.

The triangular or hexagonal shape of the indentation produced as the result of impact of the projectile as shown in Figures 26-29 is determined by the orientation of the $\{101\}$ and $\{011\}$ slip planes.

3.1.4 Slip and Crack Nucleation at Angles of Impact on the Cleavage Plane Other Than 90° .

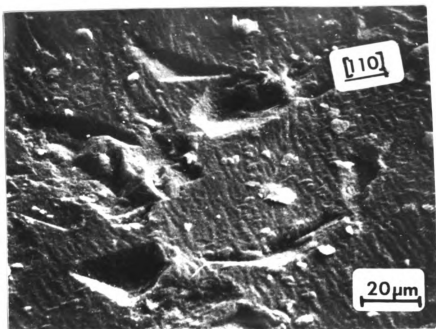
At angles of impact less than 90° , significant changes occur in the mode of erosion damage. Micromachining becomes an important mode of erosion at angles of impact greater than 30° from the normal in LiF, NaCl, and KCl.

Fig. 26. A scanning electron micrograph of:

- a. LiF eroded by 0.50 mm blunt projectiles impacting the $\{1\bar{1}0\}$ at a velocity of 45 m/s;
- b. NaCl eroded by 0.50 mm blunt projectiles impacting the $\{1\bar{1}0\}$ at a velocity of 45 m/s.

51(a)

a



b

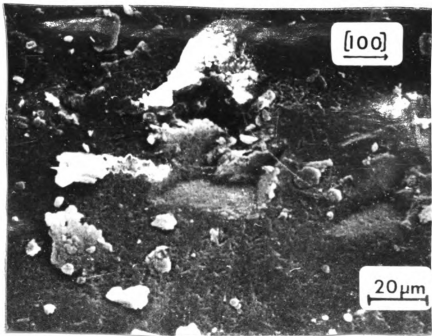


Fig. 27. A scanning electron micrograph of:

- a. KCl eroded by 0.50 mm blunt projectiles impacting the $\{1\bar{1}0\}$ at a velocity of 75 m/s;
- b. NaCl eroded by 0.50 mm blunt projectiles impacting the $\{1\bar{1}0\}$ at a velocity of 60 m/s.

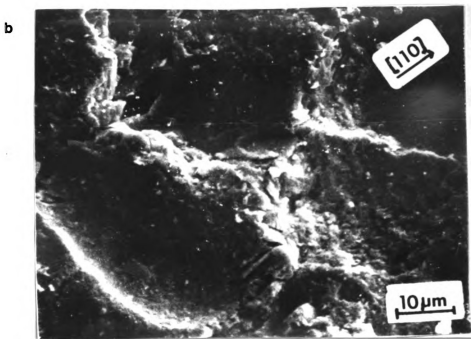


Fig. 28. A scanning electron micrograph of:

- a. LiF eroded by 0.50 mm blunt projectiles impacting the {111} at a velocity of 45 m/s;
- b. KCl eroded by 0.50 mm blunt projectiles impacting the {111} at a velocity of 45 m/s.

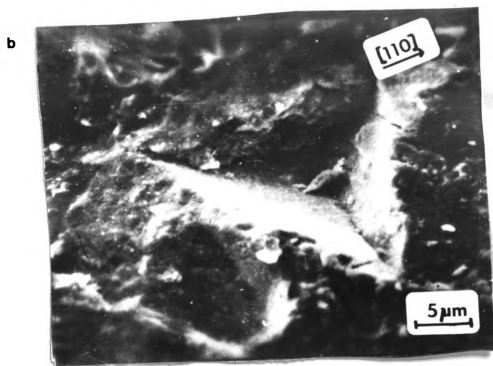
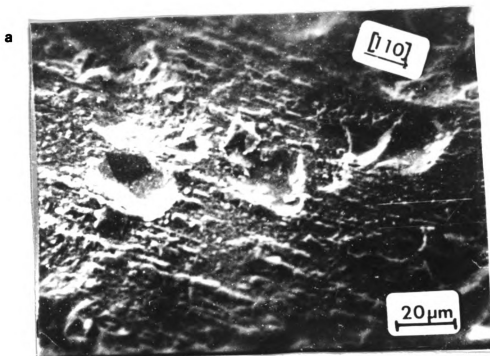
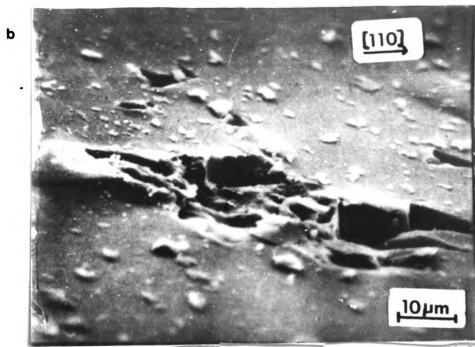
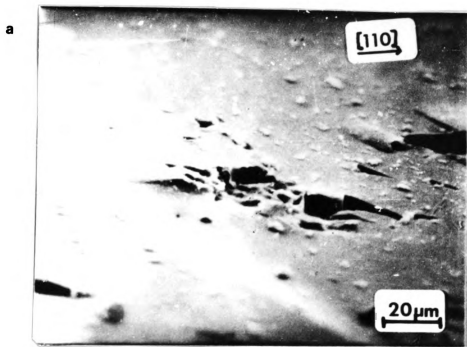


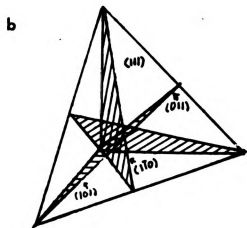
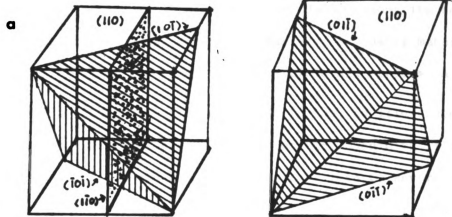
Fig. 29. A scanning electron micrograph of 0.50 mm blunt projectiles impacting the {111} at a velocity of 45 m/s ("a" is the area of contact of "b").

54(a)



- Fig. 30. a. The orientation of slip planes in NaCl structure crystals with respect to the direction of impact on the $\{110\}$.
- b. The orientation of slip planes in NaCl structure crystals with respect to the direction of impact on the $\{111\}$.

55(a)



The mode of surface damage in KCl (ductile) eroded at an angle of 60° from normal is radically different from damage produced at normal impact, as shown in Figure 31a. No large longitudinal fractures outside the line of contact are seen. During impact, the particle grazes the surface and produces surface damage along its path of travel. As the particle travels across the surface, it pushes material ahead of it which flows to the sides of the particle and produces a furrow.

Microfracturing occurs along the furrow, as illustrated in Figure 31b. Material along the path of micromachining is subjected to severe compressive and shear stresses that lead to severe work hardening of material within the path. The result of work hardening is the formation of microfractures on the $\{100\}$ family of planes (in KCl and NaCl). Long fractures are formed on the $\{100\}$ perpendicular to the direction of travel as the result of shear forces that separate the rows of microcrystals (cf. Figures 31 and 32). Material loss occurs after severe work hardening of the crystal surface as material is pushed ahead by the ploughing action of the projectile until the crystal surface is work hardened to the point of fracture. Unlike the case with more brittle materials, surface damage occurs in NaCl and KCl at velocities as low as 2 m/s.

The degree of micromachining in LiF (intermediate), as shown in Figure 33, is less extensive than in NaCl and KCl (soft materials). Unlike NaCl and KCl, LiF exhibits the formation of lateral fractures at angles of impact less than normal incidence. The number and length of these fractures are affected by the angle of impact. In normal impact on LiF, generally four equidimensional major lateral fractures are developed outside the circle of contact. The fractures are symmetric

Fig. 31. A scanning electron micrograph of KCl eroded by 0.25 mm glass beads impacting the {001} at an angle 60° from an axis normal to the surface of the crystal at a velocity of 10 m/s.

57(a)

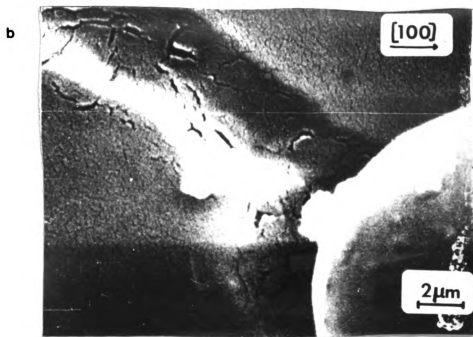
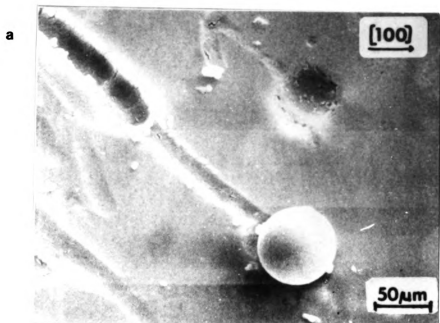
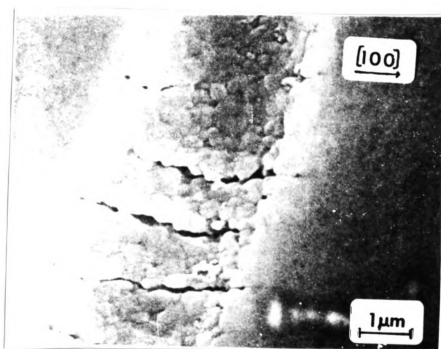
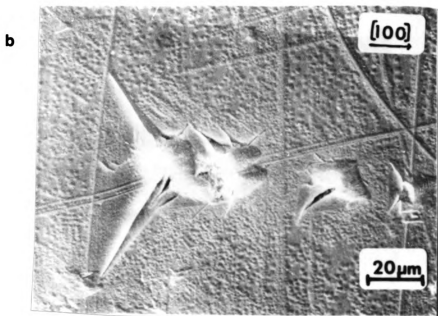
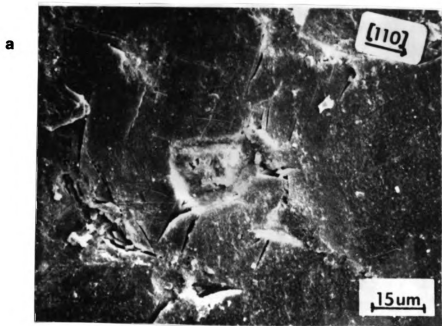


Fig. 32. A scanning electron micrograph of KCl eroded by 0.25 mm glass beads impacting the {001} at an angle 60° from an axis normal to the surface of the crystal at a velocity of 10 m/s.

58(a)



- Fig. 33. A scanning electron micrograph of LiF eroded using 0.50 mm blunt projectiles impacting the {001}:
- a. at an angle 30° from an axis normal to the surface of the crystal at a velocity of 25 m/s;
 - b. at an angle 60° from an axis normal to the surface of the crystal at a velocity of 35 m/s.



62

about the circle of contact. As the angle of impact is reduced, the length of the lateral fractures changes. At 30° from normal impact, as shown in Figure 33a, four lateral fractures are developed, but they are no longer equidimensional. The lateral fractures that are developed 120° from the direction of impact increase in length. The lateral fractures developed on the opposite side of the zone of contact decrease in length. At an angle of impact of 60° from normal, as shown in Figure 33b, only two lateral fractures are developed on the $\{110\}$ outside the circle of contact, 150° from the direction of the flow of particles. Lateral fractures are absent on the opposite side of the circle of contact as a consequence of the asymmetrical distribution of applied stress.

A limited amount of micromachining can be observed in LiF (intermediate) at angles of impact 60° from normal. A small amount of material is removed by this process, but the major mode of damage is through the development of lateral fractures.

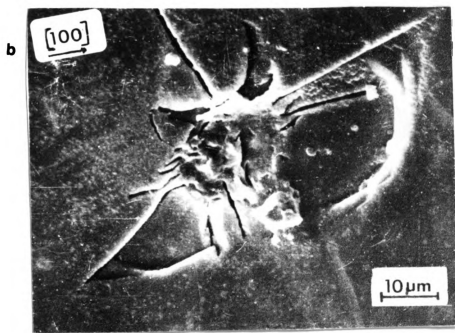
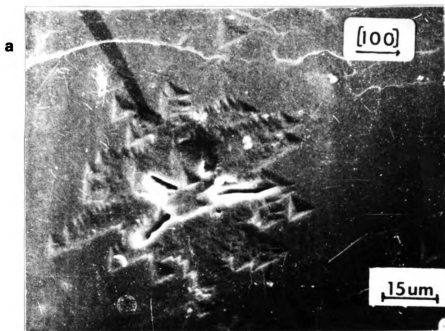
Unlike softer materials, CaF_2 (brittle) shows no micromachining for impact at an angle of 60° from normal. Although limited slip is observed, damage occurs by the development of lateral fractures. As in the case of LiF (intermediate), the length of lateral fractures shifts as the angle of impact is decreased to 60° from normal as shown in Figure 34a. The length of the lateral fractures increases with increasing velocity, as shown in Figure 34b.

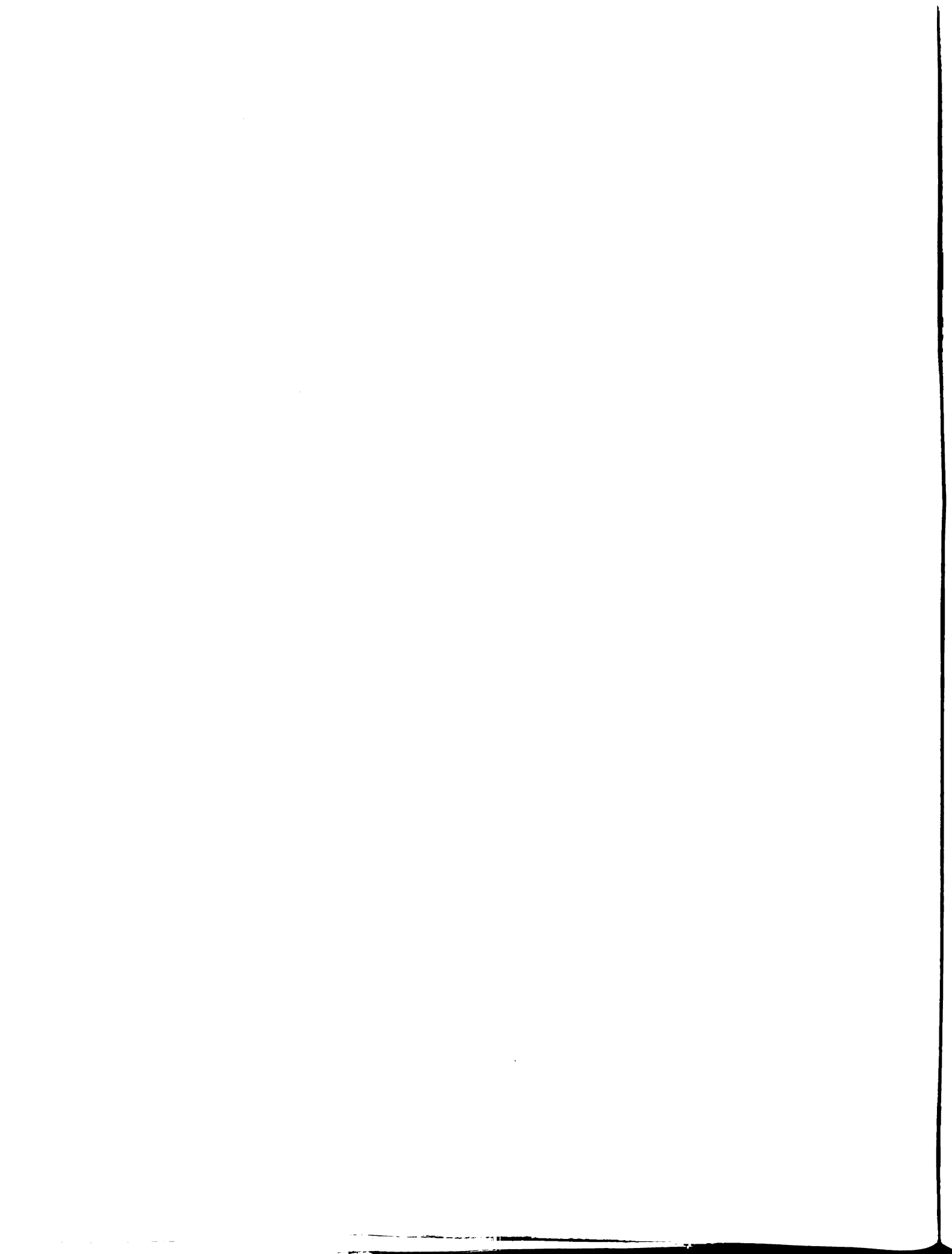
The change, as a function of the angle of impact, in the mode of erosion (from brittle to ductile damage) is dependent upon the orientation of the slip planes and the direction of the velocity.

Fig. 34. A scanning electron micrograph of CaF_2 eroded by 0.50 mm blunt projectiles impacting the {111} at an angle 60° from an axis normal to the surface of the crystal:

- a. at a velocity of 20 m/s;
- b. at a velocity of 45 m/s (etched).

61(a)





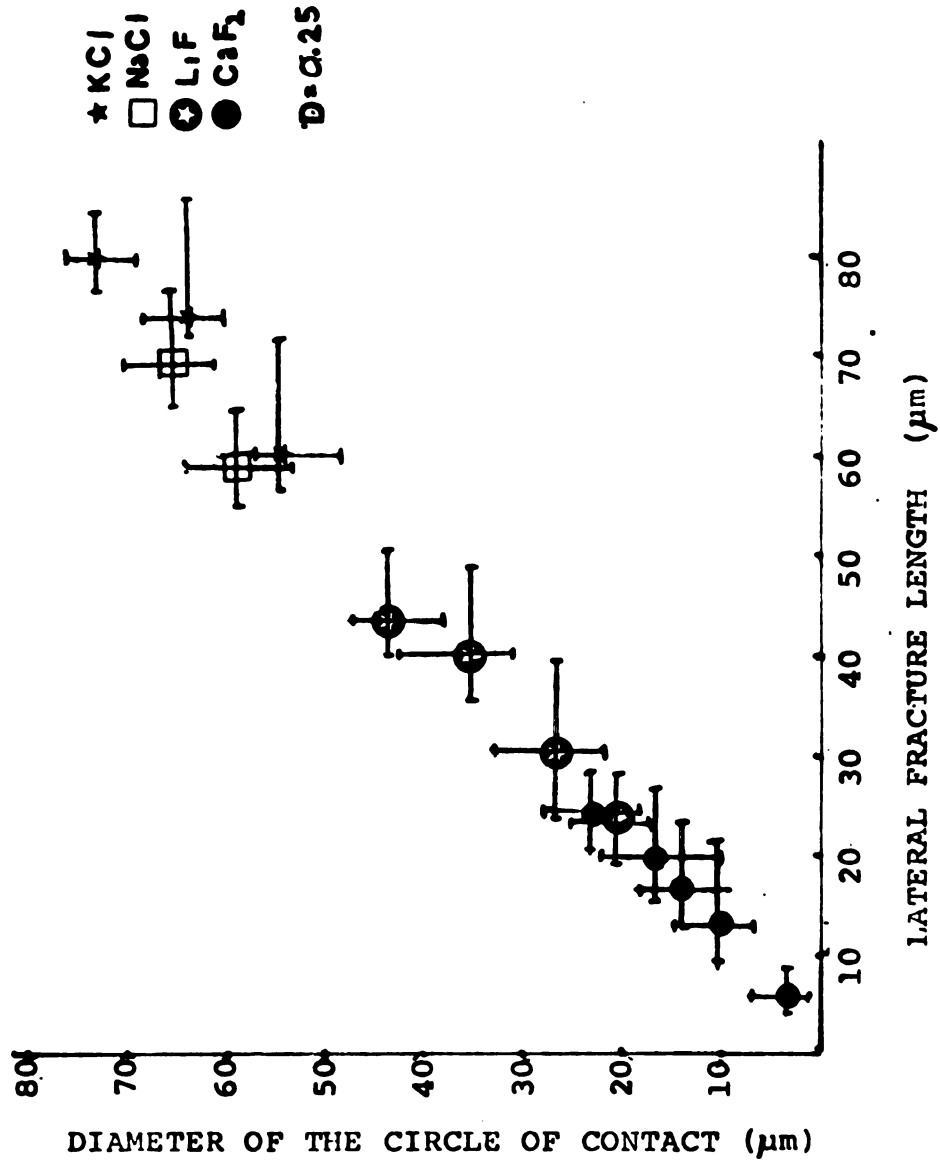
At 90° impact, the direction of the velocity is 90° from the $\langle \bar{1}\bar{1}0 \rangle$ slip directions and 60° from the $\{101\}$ slip planes. Therefore, if P is the magnitude of the impact force, the magnitude of its normal component on the $\{101\}$ and $\{001\}$ is $0.866P$. The magnitude of the shear force is $0.5P$. As the angle of impact is reduced to 60° from normal, the direction of the force of impact changes with respect to the slip planes and directions, and an increase in plastic flow in the crystal results. During this the direction of the force remains parallel to the slip direction of one $\langle 10\bar{1} \rangle$ slip direction. The normal force on a $\{101\}$ and a $\{011\}$ plane and the $\{110\}$ planes is $0.5P$. The shear force on these planes is $0.866P$. The higher magnitude of the shear force on the $\{101\}$, $\{011\}$ and $\{110\}$ slip planes leads to micromachining of the surface of the crystal.

3.1.5 The Relationship of Blunt-Projectile Damage to the Hertzian Stress Field

Several authors^{32,38,39,40,45} have suggested that Hertz's analysis of the stresses generated when an isotropic elastic sphere is pressed quasi-statically against a flat, isotropic half-space may help to predict the damage caused by the impact of a blunt projectile on the surface of a crystal. In this study, we compare the diameter of the contact zone as observed with that predicted by Hertz's analysis.

In the case of blunt-projectile damage, the intersection of major lateral fractures is a major feature. The length of the fractures increases with increasing diameter of the contact zone as shown in Figure 35.

Fig. 35. The diameter of the circle of contact versus the length of the lateral fractures.



At normal impact the diameter of the contact zone increases with impact velocity, as seen in Figure 36. The softer materials NaCl and KCl (ductile materials) show a greater increase in the diameter of the circle of contact with velocity than do CaF₂ (brittle) and LiF (intermediate). A similar increase in the contact zone with impact velocity occurs with a greater projectile diameter, as shown in Figure 37.

The diameter of the contact zone as a function of velocity was calculated by Hertz's analysis. The observed value was larger than the calculated value by a factor of about ten for CaF₂ (brittle) and LiF (intermediate), and by a factor of about twenty for KCl and NaCl (ductile) as shown in Figure 38. The discrepancy probably stems from the neglect of plastic deformation in the Hertz analysis.

Contact of a projectile on the surface of a real material is an elastic-plastic problem. Soft materials such as NaCl and KCl, which show considerable ductility, deform extensively during impact by blunt projectiles.

3.1.6 Impact Damage Produced by Sharp Projectiles

The irregular shape of sharp projectiles impacting the crystal surface make it impossible to predict the exact nature of specimen loading. During erosion, the orientation of the particle hitting the surface cannot be predicted. Several configurations are possible. As shown schematically in Figure 39, the particle could hit the crystal on a sharp corner, or on a long edge, or on a flat side. The differences are evident in the highly variable geometry of the microstructural damage, as shown in Figure 40.

Fig. 36. The diameter of the circle of contact versus the velocity of impact of 0.25 mm glass beads.

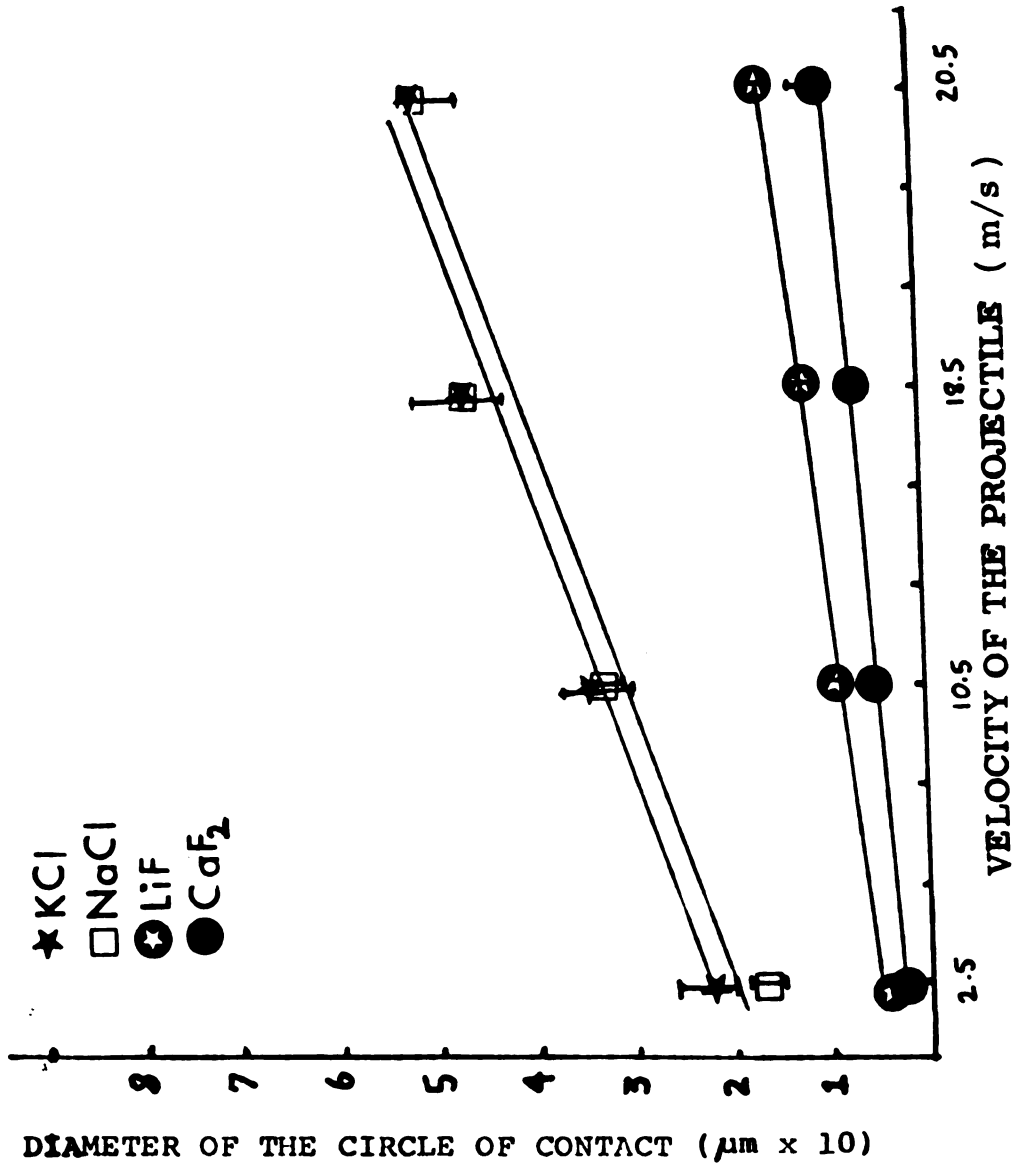


Fig. 37. The diameter of the circle of contact versus the impact velocity of 0.50 mm blunt projectiles.

66(a)

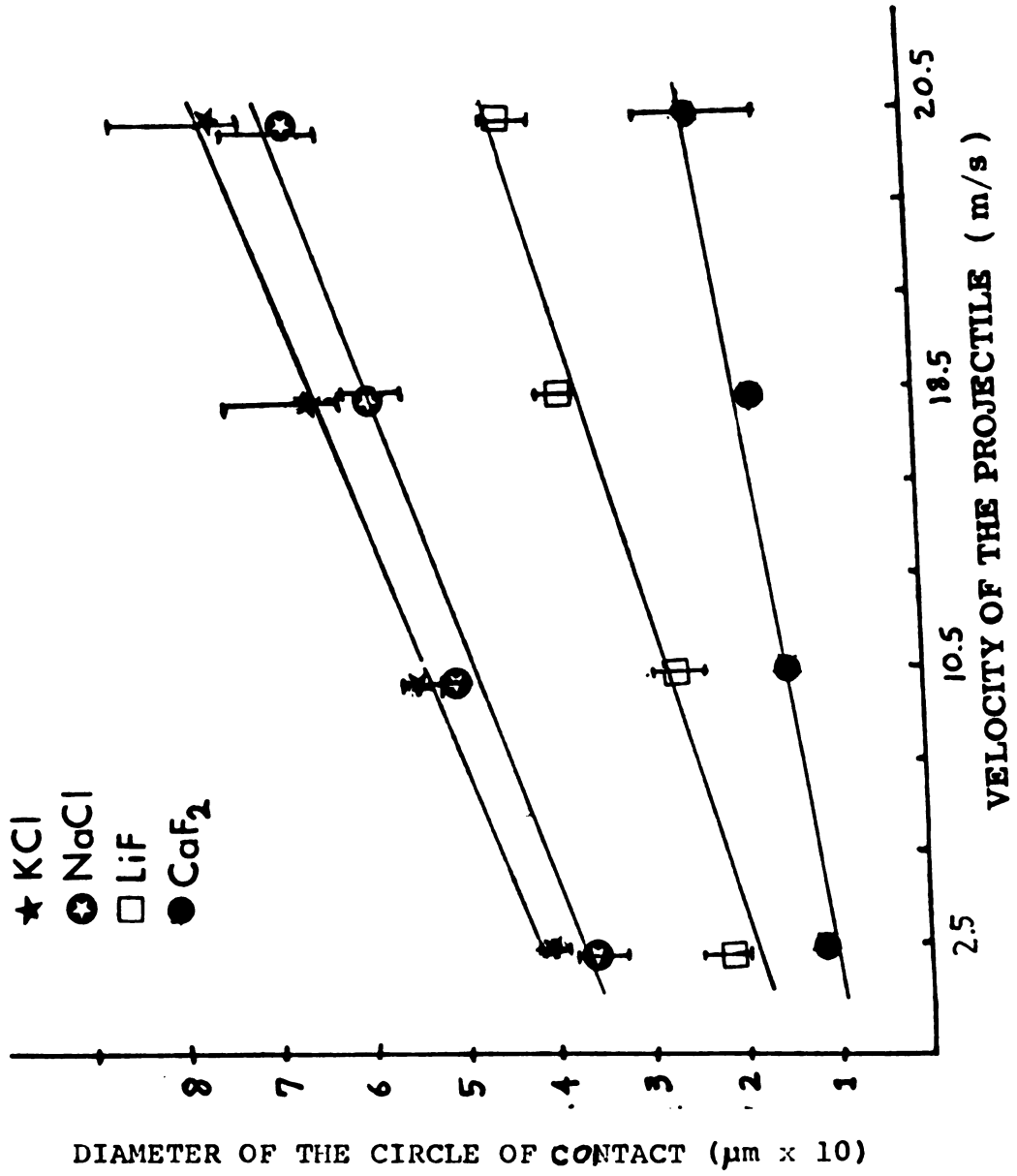


Fig. 38. The diameter of the circle of contact calculated using Hertz's analysis for contact of a spherical indenter on an isotropic medium versus the impact velocity (D =diameter of the projectile).

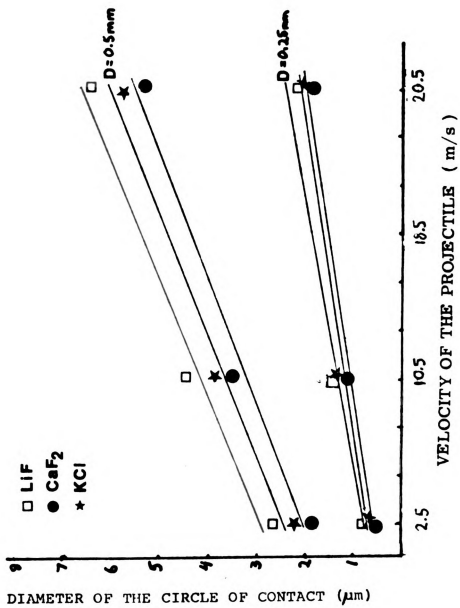


Fig. 39. Possible modes of specimen loading by sharp projectiles impacting the surface of the crystals.

- a. Point
- b. Edge
- c. Side

68(a)

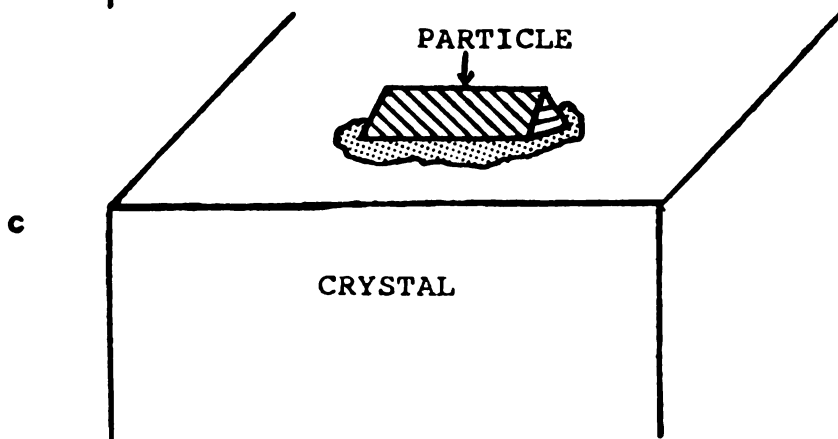
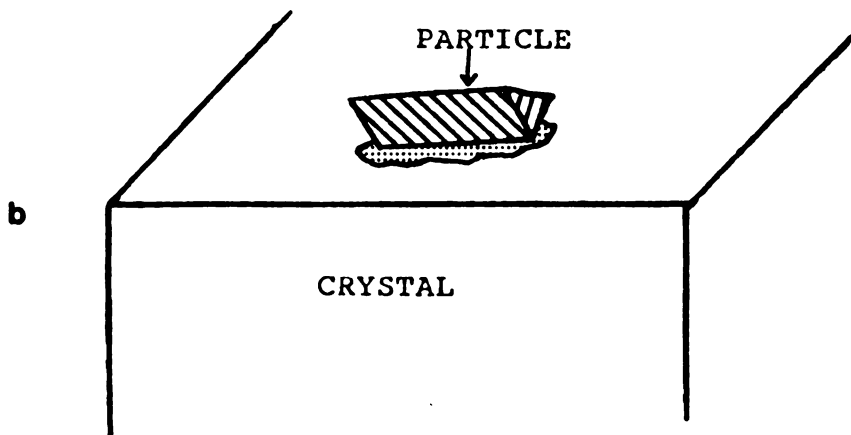
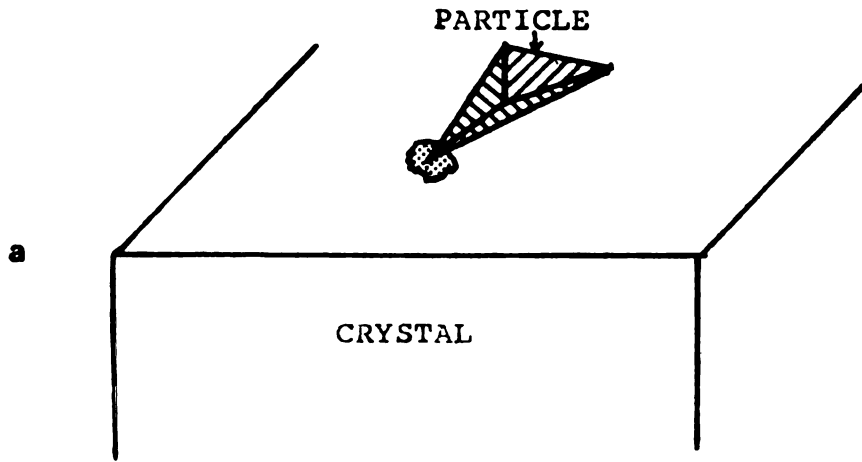
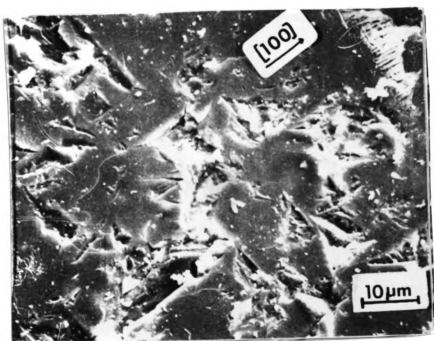


Fig. 40. A scanning electron micrograph of LiF eroded by sharp projectiles impacting the {001} at a velocity of 45 m/s.

69 (a)



Lateral fractures are not symmetric about the point of impact, in contrast with those appearing in blunt-particle impact, as shown in Figure 41a. Moreover, length of the lateral fractures cannot be predicted from the diameter of the point of impact. The mode of erosion itself appears different. The sides of the indentation produced by the impact of sharp projectiles are smooth cleavage planes, as shown in Figure 41b. The non-crystallographic microfracturing occurring in indentations by blunt projectiles is absent. In LiF (intermediate), the surfaces of the indentations are planes of the family $\{110\}$. Material loss can occur even in a single impact through formation of chips.

Similar behavior is observed in CaF_2 (brittle), as shown in Figure 42. Chipping of material is again the primary mode of material loss. The boundaries of the chips are formed by lateral fractures which are along predictable crystallographic directions.

Because of the uncertainty in predicting specimen loading, the Boussinesq field does not describe the initial stress distribution. The concentrated stress resulting from point loading results in damage by cleavage of the crystal at the point of impact.

3.2 Multiple-Impact Damage

When blunt particles strike a smooth target, the region of contact is pretty much the same for all particles, since they are more or less spherical. It is then reasonable to expect interpretable differences in erosion behavior as the angle between particle velocity and surface normal is varied. With sharp particles, however, the contact region can differ strongly from one particle to another, as say a flat side

Fig. 41. A scanning electron micrograph of LiF eroded by sharp projectiles impacting the {001}:

a. at a velocity of 20 m/s;

b. at a velocity of 45 m/s.

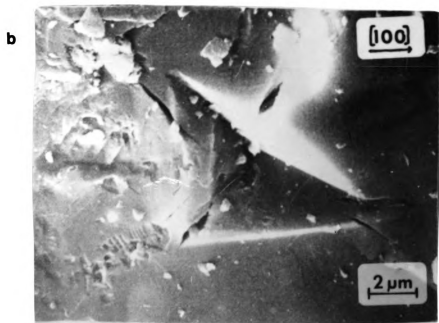
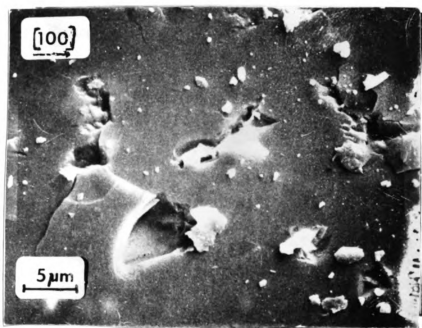


Fig. 42. A scanning electron micrograph of CaF_2 eroded by sharp projectiles impacting the $\{1\bar{1}1\}$ at a velocity of 45 m/s.



strikes in one case, and an apex or an edge in another. Consequently, quite different behavior may be expected between the two kinds of particles. Whereas microfracturing within the contact zone appears in blunt-particle damage, it is absent in sharp-particle damage. Instead, a central chip is formed at the point of impact, from which an asymmetric set of lateral fractures spreads. In contrast with blunt-particle impact, the length of these fractures cannot be predicted from the diameter of the contact zone by assuming either a Hertzian stress field or a Boussinesq stress field.

3.2.1 Impact Erosion Damage Produced by Multiple Blunt-Projectile Impact

In single-impact damage by blunt projectiles, weight loss is seldom observed. The region of damage, it will be recalled, is a zone of contact accompanied by lateral fractures along specific crystallographic directions outside the zone. In multiple impact, on the other hand, the intersection of the lateral fractures of even two single impacts can produce material loss as shown in Figure 43.

In LiF (intermediate) loss does not occur from the intersection of the lateral fractures from a pair of single impacts, as shown in Figure 44a. Instead, multiple impact in LiF results in severe plastic deformation of the surface of the material as shown in Figure 44. Extensive deformation of the surface is necessary before material loss occurs through the intersection of lateral fractures. A critical density of lateral fractures is necessary before significant material loss occurs.

In KCl and NaCl (ductile) substantial work hardening of the surface of the crystal occurs before much material loss is observed, as

Fig. 43. A scanning electron micrograph of CaF_2 eroded by 0.25 mm glass beads impacting the $\{001\}$ at a velocity of 25 m/s.

74 (a)

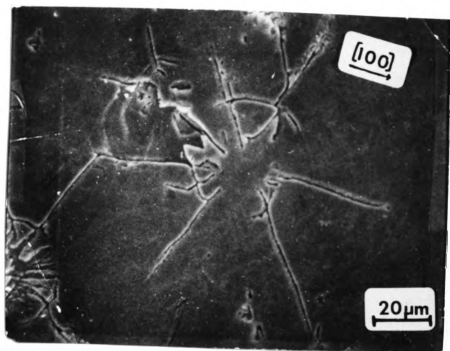
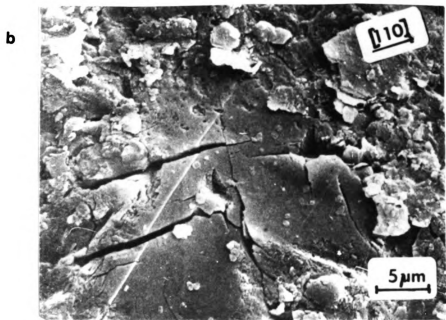
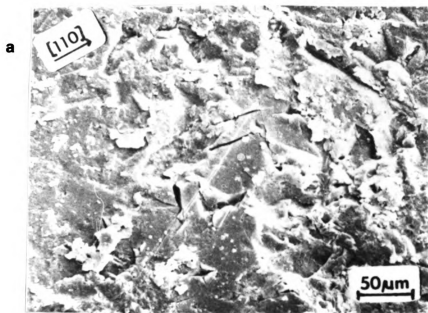


Fig. 44. A scanning electron micrograph of LiF eroded by 0.25 mm glass beads impacting the {001} at a velocity of 45 m/s.



shown in Figure 45. As in the case of LiF, a critical density of fractures is required before material is removed.

In CaF_2 (brittle) the extent of plastic deformation of the surface is considerably less, as illustrated in Figure 46. Though material loss can occur from a single impact in the form of a chip bounded by lateral fractures, it can also occur from the intersection of lateral fractures. The amount of material lost through lateral fractures is much greater than that through chips.

The plasticity of the material affects the rate of erosion of the material, as shown in Figure 47. NaCl and KCl, which show greater plasticity, have a lower rate of erosion than either CaF_2 (brittle) or LiF (intermediate). The high rate of erosion for CaF_2 may be due to material loss resulting from the intersection of a single set of lateral fractures, or the chipping of material from the surface by the action of a single projectile. The rate of erosion increases with the projectile size, as shown in Figure 48, possibly as the result of an increase in the length of lateral fractures with the increase in projectile diameter.

Loss of material occurs through the intersection of fractures on the {010} as shown in Figure 16. The mode is similar to that observed by Adler⁴⁵ for the erosion of glass by blunt projectiles. The mode appears to apply best to brittle materials such as CaF_2 . In the case of ductile materials such as NaCl and KCl, the rate of erosion is dependent upon the density of fractures. Fracture extension is also observed during erosion. This cannot be accounted for in Adler's model. As the velocity of impact is increased, large fractures are developed

Fig. 45. A scanning electron micrograph of KCl eroded by 0.25 mm glass beads impacting the {001} at a velocity of 75 m/s.

77(a)



Fig. 46. A scanning electron micrograph of CaF_2 eroded by 0.25 mm glass beads impacting the $\{111\}$ at a velocity of 75 m/s.

78(a)

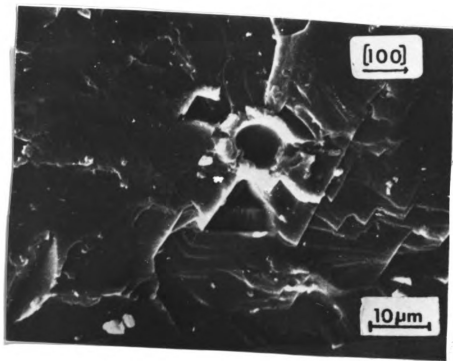


Fig. 47. The rate of erosion versus the impact velocity of 0.25 mm projectiles impacting the {001} in NaCl, KCl and LiF, and the {111} in CaF₂.

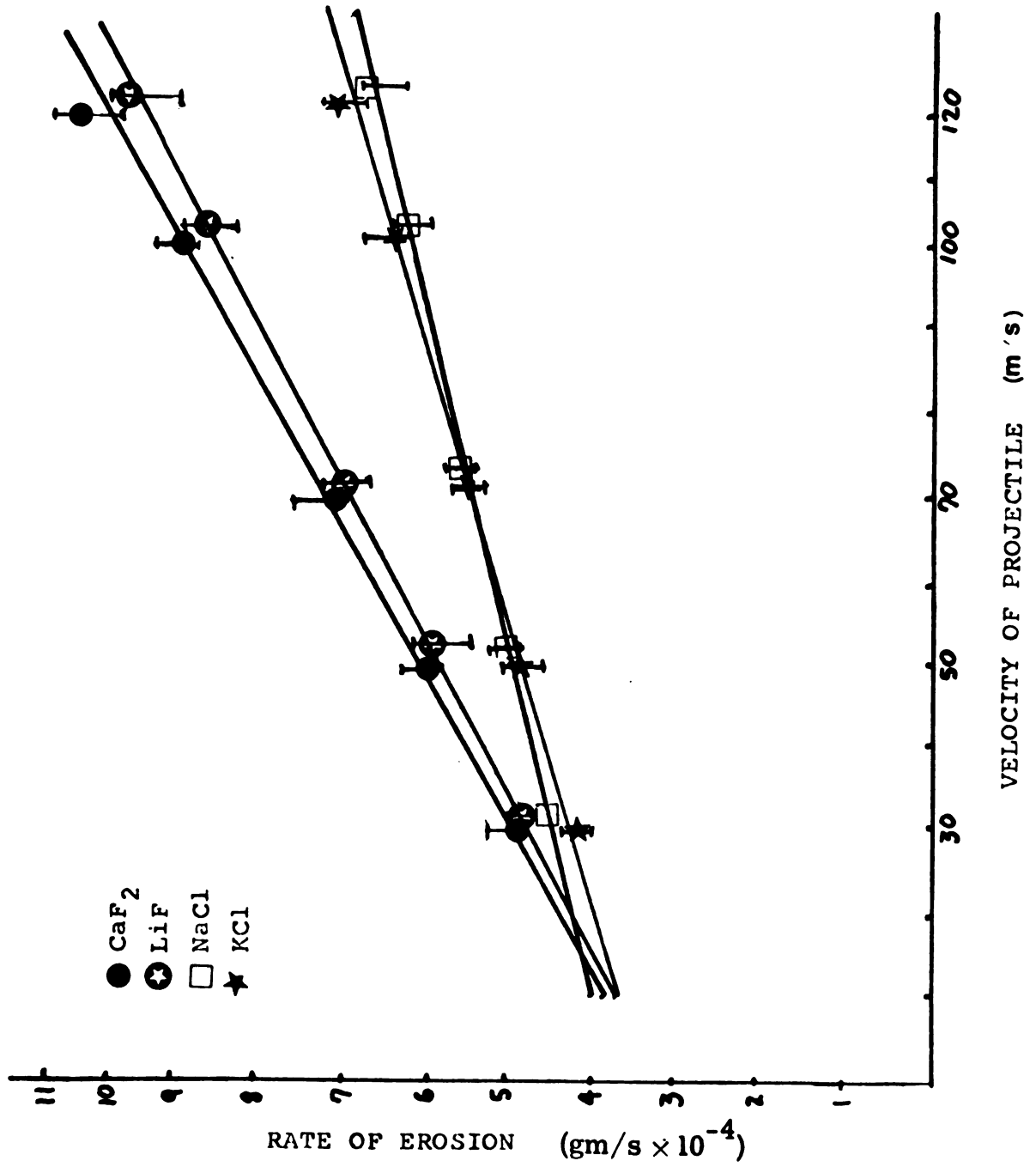


Fig. 47. The rate of erosion versus the impact velocity of 0.25 mm projectiles impacting the {001} in NaCl, KCl and LiF, and the {111} in CaF₂.

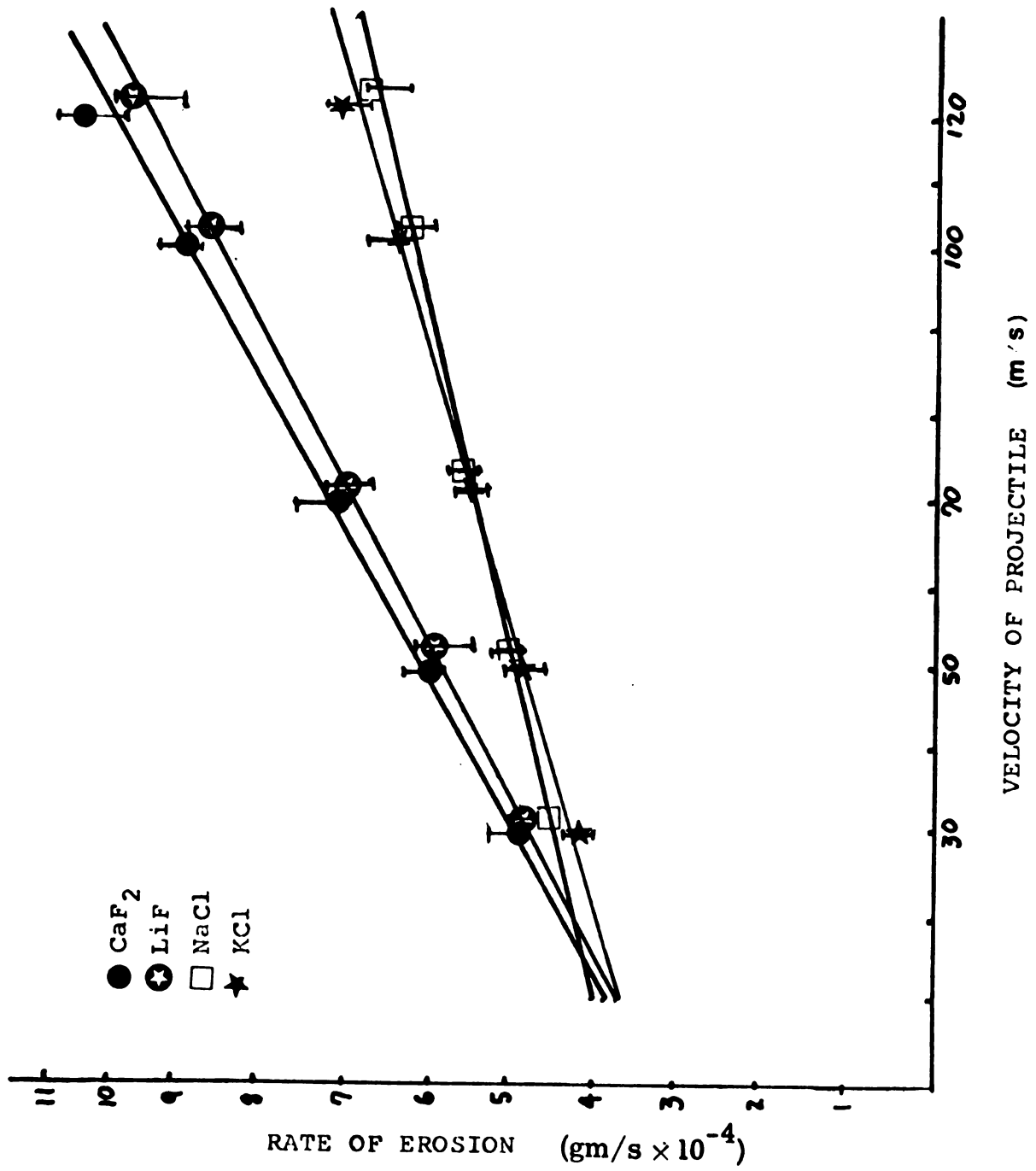
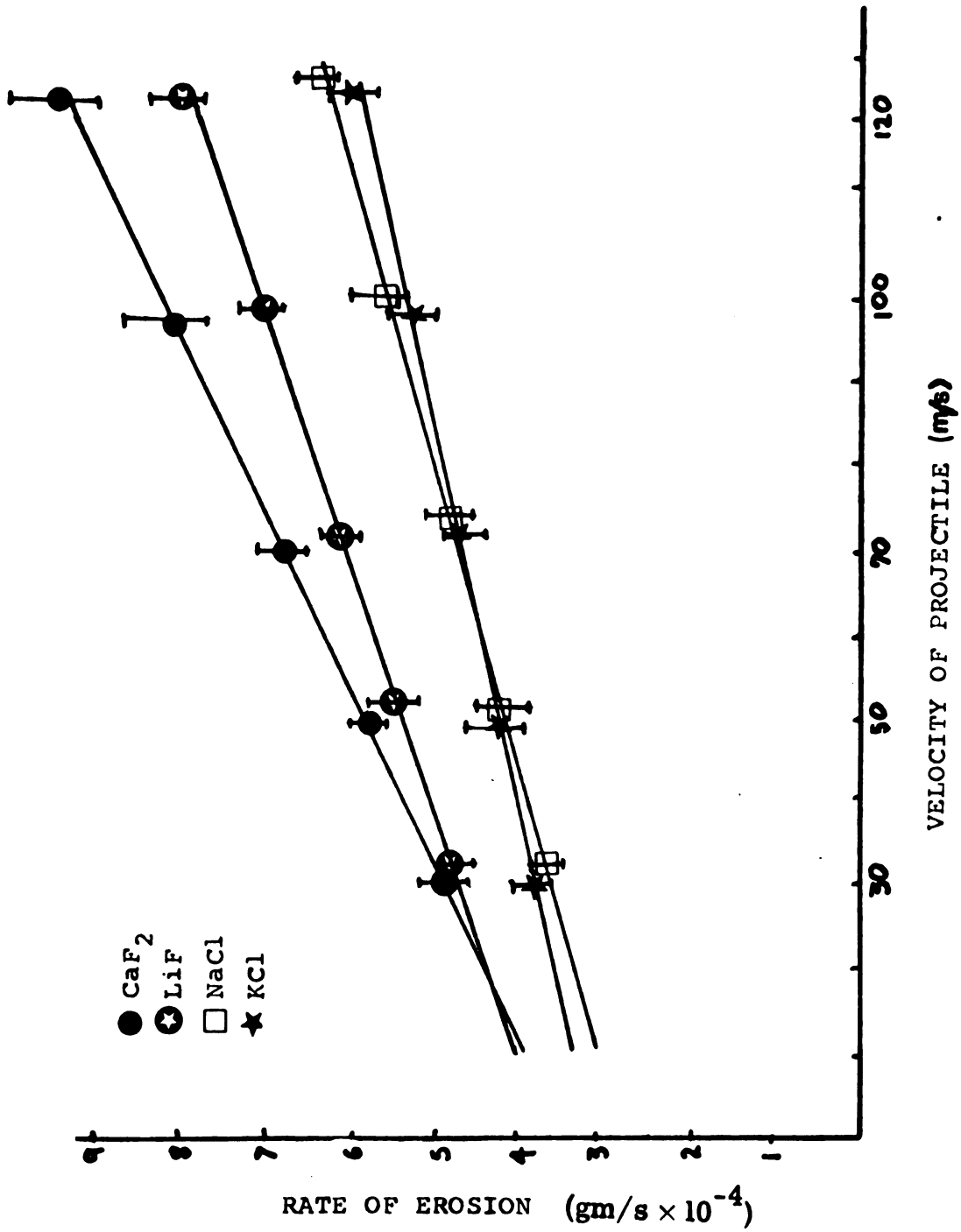


Fig. 48. The rate of erosion versus the impact velocity of 0.50 mm projectiles impacting the {001} in NaCl, KCl, and LiF, and the {111} in CaF₂.



along cleavage planes through fracture extension. These fractures result in the loss of large volumes of material from the surface, as shown in Figure 49. Plastic deformation is confined to the region near the surface of the crystal, as shown in Figure 50. As material is removed, a new, largely undisturbed surface is exposed to further erosion.

As the angle of impact departs from 90° (normal incidence) the location and the length of the lateral fractures change. In LiF (intermediate), NaCl (ductile) and KCl (ductile), micromachining becomes an important mode of surface damage. The erosion rate decreases with impact angle, as shown in Figure 51, as a result of increased plastic flow.

In LiF (intermediate), KCl (ductile) and NaCl (ductile) the rate of erosion for impact on the $\{110\}$ is less than that for impact on the $\{100\}$ as shown in Figure 52. Severe roughening of the surface occurs before material loss occurs, as shown in Figure 53a. Lateral fractures are observed only after severe deformation of the surface in KCl (ductile) as shown in Figure 53b. Similar behavior is observed in LiF (intermediate), where severe plastic deformation occurs before material loss, as shown in Figure 54. The effect of the increase in plastic flow cannot be accounted for by Adler's model.

3.2.2 Impact-Erosion Damage Produced by Multiple Sharp-Projectile Impact

Damage by sharp projectiles can be characterized by material loss from single impacts. As a sharp projectile hits the surface, lateral fractures develop along specific crystallographic directions. Material loss then occurs through the formation on chips bounded by these

Fig. 49. A scanning electron micrograph of KCl eroded by 0.25 mm glass beads impacting the {001} at a velocity of 75 m/s.

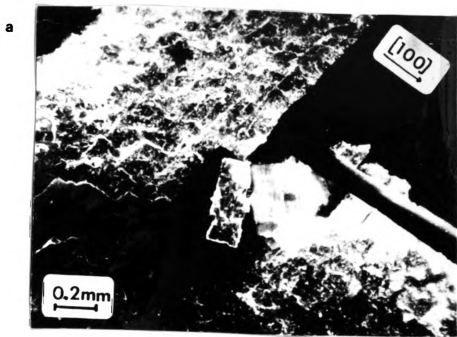


Fig. 50. A scanning electron micrograph of KCl eroded by 0.25 mm glass beads impacting the {001} at a velocity of 75 m/s.

83(a)



Fig. 51. The rate of erosion versus the impact velocity of 0.25 mm projectiles impacting the {001} in NaCl, KCl, and LiF, and {111} in CaF_2 at an angle of 60° from an axis normal to the surface of the crystal.

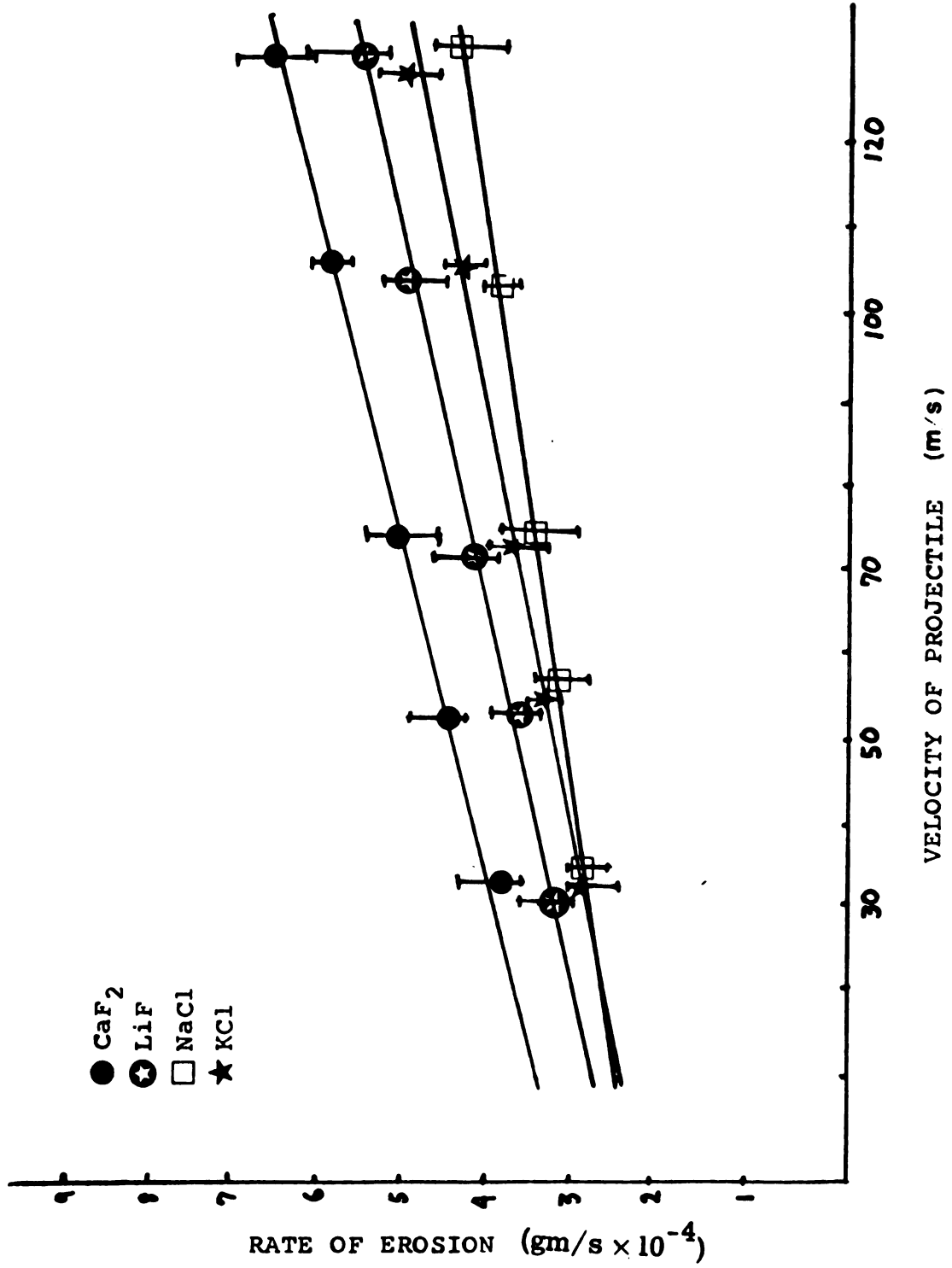




Fig. 52. The rate of erosion versus the impact velocity of 0.25 mm projectiles impacting the $\{1\bar{1}0\}$.

85(a)

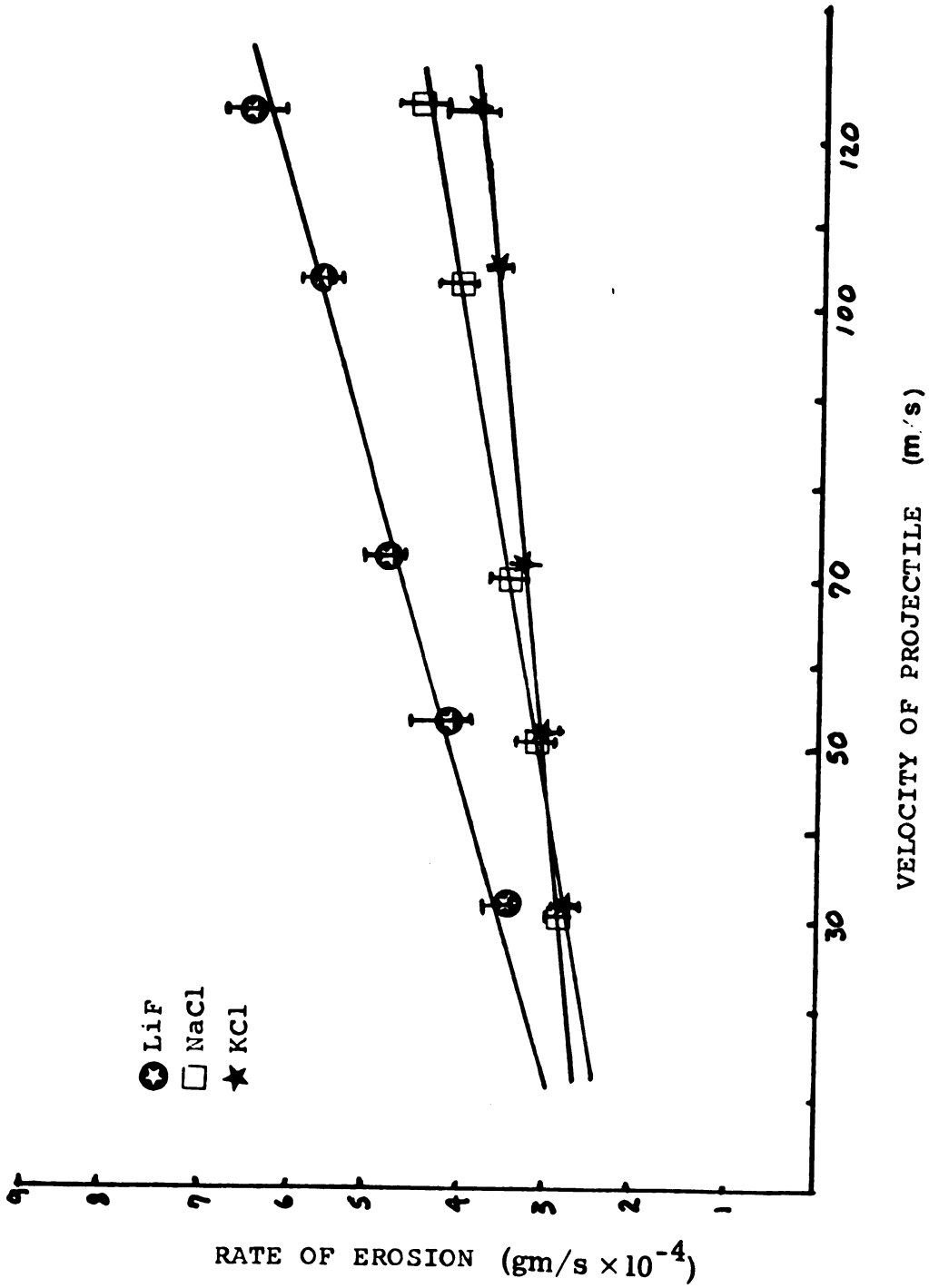


Fig. 53. A scanning electron micrograph of KCl eroded by 0.50 mm blunt projectiles impacting the $\{1\bar{1}0\}$ at a velocity of 75 m/s.

86(a)

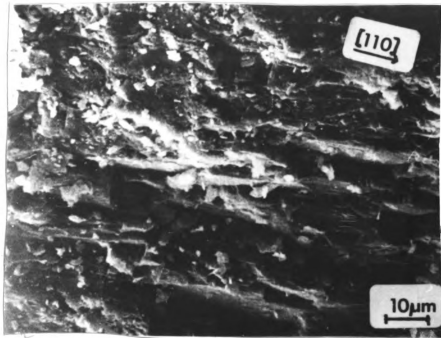
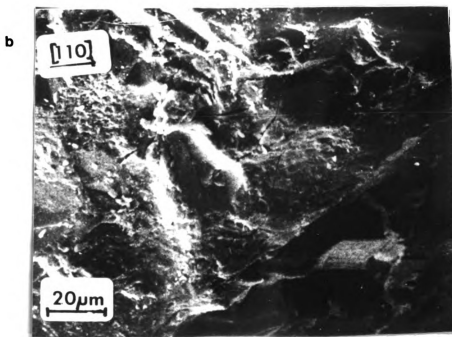
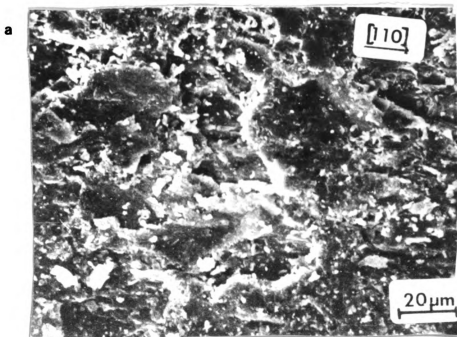


Fig. 54. A scanning electron micrograph of LiF eroded by 0.50 mm blunt projectiles impacting the $\{1\bar{1}0\}$ at a velocity of 75 m/s.

87(a)

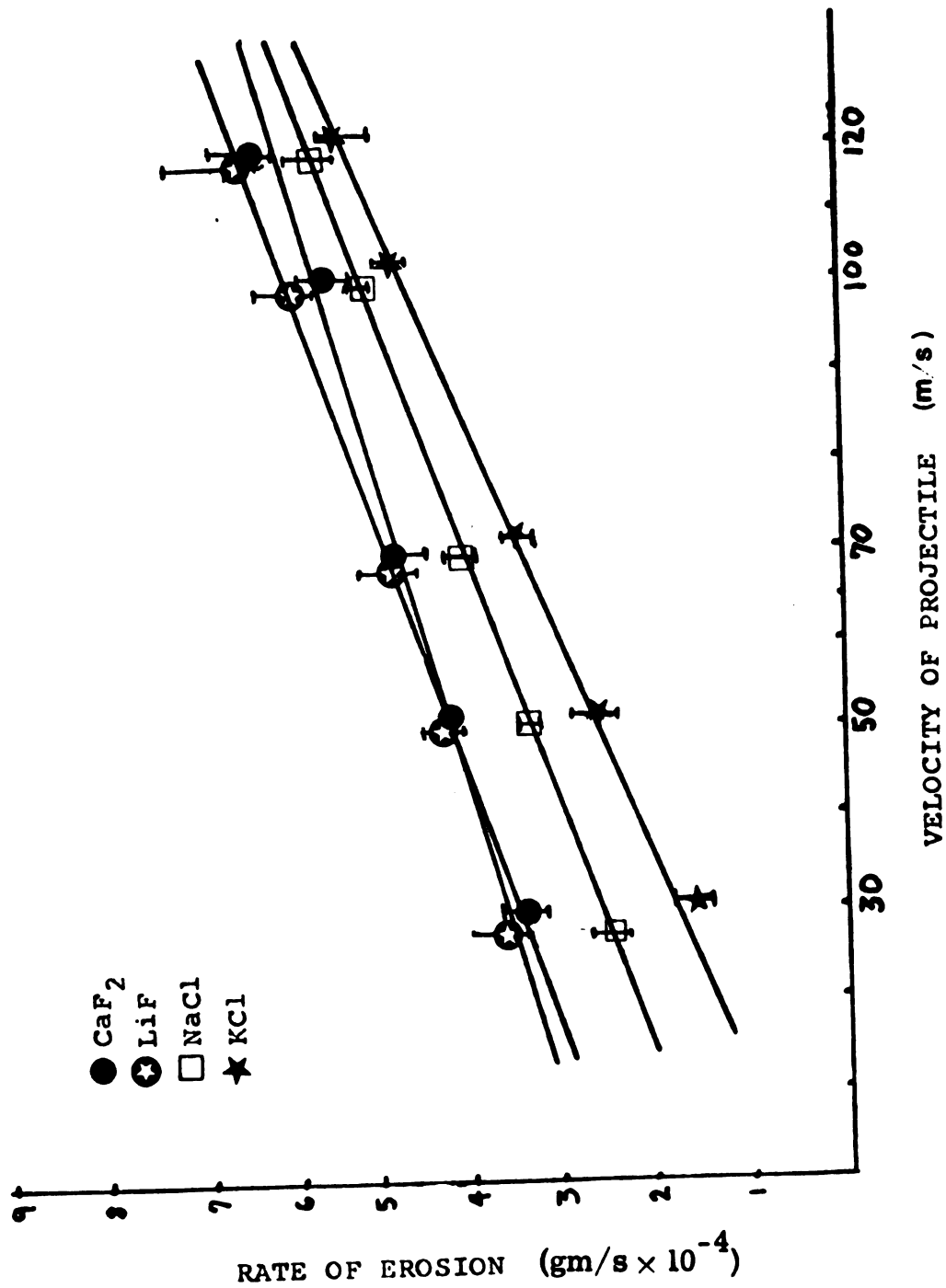


lateral fractures. The damage produced by single impact is confined to the region near the surface of the crystal. In LiF (intermediate) and CaF_2 (brittle) extensive surface damage occurs as the result of multiple impact of sharp projectiles and results in relatively high rates of erosion as shown in Figure 55. The rate of erosion increases with velocity in LiF, NaCl, KCl, less so in CaF_2 . The high rate of erosion is due, in part, to weight loss occurring through the result of a single impact. Weight loss may be predicted as the result of single, independent impacts or events. This approach was taken by Hockey et al.²² in the prediction of erosion behavior of glass by sharp projectiles.

As in metals, erosion in halide single crystals is characterized by an incubation period. Unlike the case in metals, a true steady-state period was not observed. As erosion proceeds, fracture extension results in the massive loss of material, as observed by Hoff et al.²¹ The incubation period in halide single crystals rises with the ductility of the material. A critical density of cracks is necessary before material loss occurs.

The erosion damage produced by blunt projectiles takes place by a different mechanism from that produced by sharp projectiles. With sharp projectiles, damage is the result of the accumulation of random single impacts. With blunt projectiles it is the result of the intersection of lateral fractures, as proposed by Adler.⁴⁵ In plastic materials, however, the resistance to erosion is greater than that predicted by him.

Fig. 55. The rate of erosion versus the impact velocity of SiC powder impacting the {001} in NaCl, KCl, and LiF, and the {111} in CaF₂.



4. CONCLUSIONS

SINGLE-IMPACT DAMAGE

Blunt Projectile

1. Damage produced by single normal impact of blunt projectiles is characterized by a contact zone and a set of lateral fractures occurring outside this zone. The contact zone shows damage by extensive plastic flow and intense microfracturing. In contrast, the lateral fractures, which occur as the result of the interaction of dislocations, lie exclusively along specific crystallographic directions. Although the damage superficially resembles a Hertzian cone fracture, the damage differs in that lateral fractures do not follow the path predicted by the Hertzian stress field, and the contact zone is characterized by massive plastic flow.
2. In LiF, normally impacted on the cleavage plane, the mode of damage within the contact zone changes between 25°C and elevated temperatures (200°C and 400°C). Microfracturing is absent at elevated temperatures, and the contact zone has a faceted appearance.
3. The length of the lateral fractures in normal impact is proportional to the diameter of the contact zone, which increases more or less linearly with velocity. For CaF₂ (brittle) and LiF (intermediate), the length of the lateral fractures is lower by a factor of ten or so than that estimated by Hertz's analysis of contact of a sphere on an elastic isotropic material. For KCl and NaCl

- (ductile), the discrepancy is even greater, by a factor of twenty or so. This larger factor is presumably due to the higher ductility of KCl and NaCl.
4. The critical threshold velocity for microscopic damage to appear upon normal impact depends on the ductility of the material. This velocity is greatest in CaF_2 (brittle) and least in KCl and NaCl (ductile). For LiF (intermediate) it lies between the velocities for CaF_2 and KCl.
 5. The mode of erosion in normal impact depends on the crystallographic orientation of the plane impacted. Damage on the $\{110\}$ and $\{111\}$ in NaCl-structure crystals is characterized by a faceted contact zone within which microfracturing is absent. In contrast, damage on the $\{001\}$ in such crystals is characterized by brittle fracture. This change in the mode of damage for impact on the $\{110\}$ and $\{111\}$ is due to the changed orientation of the direction of slip with respect to the direction of displacement of material as the result of impact.
 6. As the angle of impact is decreased from 90° , the location and the length of the lateral fractures shift. Micromachining, as proposed by Finnie, becomes an important mode of surface damage in impact at 60° in KCl and NaCl (ductile). The importance of micromachining decreases with ductility of the material, however, and in LiF (intermediate) and CaF_2 (brittle) the intersection of lateral fractures remains as the major mode of material loss.

Sharp Projectiles

7. When blunt particles strike a smooth target, the region of contact is pretty much the same for all particles, since they are more or

less spherical. It is then reasonable to expect interpretable differences in erosion behavior as the angle between particle velocity and surface normal is varied. With sharp particles, however, the contact region can differ strongly from one particle to another, as say a flat side strikes in one case, and an apex or an edge in another. Consequently, quite different behavior may be expected between the two kinds of particles. Whereas microfracturing within the contact zone appears in blunt-particle damage, it is absent in sharp-particle damage. Instead, a central chip is formed at the point of impact, from which an asymmetric set of lateral fractures spreads. In contrast with blunt-particle impact, the length of these fractures cannot be predicted from the diameter of the contact zone by assuming either a Hertzian stress field or a Boussinesq stress field.

MULTIPLE-IMPACT DAMAGE

Blunt Projectile

8. Material loss is dependent upon the density of fractures. In CaF_2 (brittle), material loss can occur upon the intersection of only a pair of lateral fractures. Decrease in the hardness of the material increases the number of lateral fractures required for material loss to occur.
9. Fracture extension occurs at greater impact velocities. This fracture extension results in massive material loss, as observed by Hoff et al. in glass.

10. Higher ductility results in a lower rate of erosion inasmuch as the ductility of a single crystal depends upon the angle of the applied stress to potential slip planes, the rate of erosion depends on the orientation of the sample as well as the temperature of the material.

Sharp Projectile

11. In contrast with material loss from impact by blunt projectiles--where loss occurs only from the intersection of lateral fractures from different centers--damage can result also from the formation of chips mentioned in item 7, in addition to the loss by fracture intersection.

APPENDIX

TABLE A.1 Diameter of the zone of contact and the length of lateral fractures in crystals eroded by 0.25 mm glass beads impacting the {001} in NaCl, KCl, LiF and the {111} in CaF₂. (counts/sample = 10)

Material	Diameter of the Zone of Contact (μm)			Lateral Fracture Length (μm)		
	Average	Minimum	Maximum	Average	Minimum	Maximum
KCl	73	69	76	80	78	84
	64	60	69	73	71	85
	54	49	59	60	58	71
NaCl	65	61	70	70	65	77
	60	53	62	59	55	62
LiF	42	38	47	42	40	50
	35	31	41	40	35	48
	28	22	31	30	23	40
	20	19	26	21	19	28
CaF ₂	22	19	29	25	20	28
	18	10	22	20	15	28
	14	10	18	17	15	21
	10	8	15	12	9	21
	3	2	7	5	4	9

TABLE A.2 Diameter of the zone of contact versus the velocity of 0.25 mm glass beads impacting the {001} in NaCl, KCl, and LiF and the {111} in CaF₂. (counts/sample = 10)

Material	Velocity (m/s)	Average diameter of the zone of contact (x 10 ⁻² mm)		
KCl	2.2	1.0	0.6	0.7
	2.4	2.1	2.4	2.0
	10.4	3.5	3.2	3.6
	18.5	4.7	4.6	4.6
	26.5	5.0	5.4	5.2
NaCl	2.2	1.1	1.1	1.0
	2.4	1.8	1.9	1.8
	10.4	3.3	2.6	3.5
	18.5	4.8	4.6	5.1
	26.5	5.1	5.2	5.2
LiF	2.2	-	-	-
	2.4	0.2	0.2	0.1
	10.4	0.7	0.7	1.1
	18.5	1.2	1.2	1.3
	26.5	1.6	1.6	1.7
CaF ₂	2.2	-	-	-
	2.4	0.2	-	0.1
	10.4	0.5	0.8	0.6
	18.5	0.8	0.7	1.0
	26.5	1.1	1.0	0.7

TABLE A.3 Diameter of the zone of contact versus the velocity of 0.50 mm blunt projectiles impacting the {001} in NaCl, KCl, and LiF and the {111} in CaF₂. (counts/sample = 10)

Material	Velocity (m/s)	Average diameter of the zone of contact (x 10 ⁻² mm)		
KCl	2.2	2.5	2.3	2.2
	2.4	4.0	4.1	4.0
	10.4	5.9	6.0	5.7
	18.5	6.5	6.9	7.1
	26.5	8.5	8.0	7.9
NaCl	2.2	3.1	3.0	3.0
	2.4	3.9	3.7	3.6
	10.4	5.1	5.0	5.1
	18.5	6.0	6.2	5.9
	26.5	7.0	7.0	6.7
LiF	2.2	1.0	0.6	0.5
	2.4	2.4	2.0	2.0
	10.4	3.1	2.8	2.6
	18.5	4.0	3.9	3.9
	26.5	4.5	4.4	4.7
CaF ₂	2.2	0.2	0.3	0.3
	2.4	1.2	1.0	1.1
	10.4	1.8	1.5	1.5
	18.5	2.0	2.0	2.0
	26.5	2.6	2.7	2.2

TABLE A.4 Diameter of the zone of contact versus the velocity calculated using Hertz's analysis for contact of a spherical indenter on an isotropic medium.

Material	Particle Diameter (mm)	Velocity (m/s)	Diameter of zone of contact ($\times 10^{-3}$ mm)
KCl	0.5	2.4	2.1
		10.4	4.0
		26.5	5.9
LiF		2.4	3.8
		10.4	4.6
		26.5	6.8
CaF ₂		2.4	1.9
		10.4	3.5
		26.5	5.5
KCl	0.25	2.4	0.9
		10.4	1.3
		26.5	2.1
LiF		2.4	0.9
		10.4	1.5
		26.5	2.4
CaF ₂		2.4	0.5
		10.4	1.1
		26.5	1.8

TABLE A.5 The rate of erosion versus the impact velocity of 0.25 mm glass beads impacting the {001} in NaCl, KCl, and LiF and {111} in CaF₂. *

Material	Velocity (m/s)	Rate of Erosion (gm/s x 10 ⁻⁴)				
NaCl	30	3.3	3.4	3.3	3.5	3.3
	50	4.0	4.3	4.0	4.2	3.8
	70	4.8	4.9	4.8	4.7	4.5
	100	5.6	6.0	5.4	5.9	5.5
	120	5.8	5.9	5.8	5.8	5.5
KCl	30	3.5	3.2	3.3	3.3	3.3
	50	4.1	3.5	3.6	4.0	3.2
	70	4.5	4.2	4.6	4.5	4.1
	100	5.1	5.0	5.4	5.0	5.3
	120	5.9	5.1	5.6	5.8	5.1
LiF	30	4.5	4.1	4.6	4.2	4.3
	50	5.2	5.0	5.3	5.0	5.0
	70	5.9	5.8	6.0	5.8	5.8
	100	7.0	6.7	7.1	6.7	6.9
	120	7.4	7.0	8.2	7.5	7.2
CaF ₂	30	4.4	4.6	4.9	5.0	4.4
	50	5.4	5.7	5.9	5.8	5.9
	70	6.5	6.8	6.9	6.7	6.8
	100	7.9	8.2	8.0	8.5	8.0
	120	8.4	8.6	9.0	8.6	8.5

* Number of Samples/Entry = 4

TABLE A.6 The rate of erosion versus the impact velocity of 0.50 mm blunt projectiles impacting the {001} in NaCl, KCl, and LiF and {111} in CaF₂. *

Material	Velocity (m/s)	Rate of Erosion (gm/s x 10 ⁻⁴)				
NaCl	30	4.5	4.1	4.1	4.3	4.4
	50	4.8	5.0	4.9	4.4	4.9
	70	5.4	5.3	5.1	5.3	5.2
	100	5.9	6.2	6.0	6.0	6.1
	120	6.2	6.1	6.1	5.8	6.0
KCl	30	4.2	4.0	4.2	4.0	4.1
	50	5.0	4.3	4.5	4.9	5.0
	70	5.3	5.2	5.2	5.2	5.1
	100	6.3	6.0	6.4	6.1	6.0
	120	6.5	7.1	6.6	6.6	6.5
LiF	30	4.8	4.2	4.6	4.8	4.7
	50	5.9	5.2	5.8	5.7	5.7
	70	6.6	6.3	6.4	6.3	6.4
	100	8.1	8.0	8.1	7.8	8.0
	120	8.5	9.3	9.0	8.8	8.4
CaF ₂	30	5.0	4.5	4.6	4.8	4.8
	50	5.9	5.8	5.8	6.0	5.9
	70	6.9	6.8	6.7	6.8	6.8
	100	8.4	8.0	8.5	8.7	8.0
	120	9.2	10.2	9.3	9.0	9.2

* Number of Samples/Entry = 4

TABLE A.7 The rate of erosion versus the impact velocity of 0.25 mm glass beads impacting the {001} in NaCl, KCl, and LiF and {111} in CaF₂ at an angle 60° from an axis normal to surface of the crystal. *

Material	Velocity (m/s)	Rate of Erosion (gm/s x 10 ⁻⁴)				
NaCl	30	2.9	3.0	2.8	2.9	2.9
	50	3.1	3.0	3.1	3.0	3.0
	70	3.5	3.4	4.0	3.5	3.5
	100	4.1	3.9	4.4	4.1	4.3
	120	4.5	4.4	5.0	4.6	4.6
KCl	30	2.4	2.8	2.8	2.6	2.6
	50	3.0	3.2	2.9	2.9	3.1
	70	2.9	3.2	3.2	3.0	3.2
	100	2.9	3.9	3.9	3.9	3.8
	120	3.6	4.0	4.3	4.1	4.0
LiF	30	3.0	3.2	4.0	3.3	3.1
	50	3.8	3.3	4.0	3.5	3.4
	70	4.0	3.8	4.7	4.0	4.3
	100	4.9	5.0	4.8	4.4	4.8
	120	5.1	4.9	5.9	5.2	4.9
CaF ₂	30	4.0	3.5	4.0	4.3	4.2
	50	4.2	5.0	4.5	4.6	4.6
	70	5.0	4.5	5.5	5.1	5.0
	100	5.5	5.8	5.8	6.1	5.9
	120	6.2	6.9	5.8	6.3	6.1

* Number of Samples/Entry = 4

TABLE A.8 The rate of erosion versus the impact velocity of 0.25 mm projectiles impacting the {110}.*

Material	Velocity (m/s)	Rate of Erosion (gm/s x 10 ⁻⁴)				
NaCl	30	2.9	2.7	2.8	2.8	2.7
	50	3.0	3.1	3.0	3.1	3.1
	70	3.3	3.1	3.4	3.3	3.4
	100	3.9	4.1	3.8	3.7	3.9
	120	4.0	4.4	4.2	4.2	4.1
KCl	30	2.8	2.9	2.9	2.7	2.7
	50	2.7	2.7	2.6	2.7	2.5
	70	3.2	3.4	3.2	3.1	3.1
	100	3.5	3.4	3.5	3.5	3.5
	120	3.4	4.0	3.3	3.3	3.7
LiF	30	3.5	3.3	3.3	3.4	3.5
	50	4.3	4.0	3.8	3.9	3.5
	70	4.4	4.2	4.0	4.1	4.0
	100	5.8	5.6	5.4	5.5	5.7
	120	6.0	6.7	5.9	5.9	6.0

* Number of Samples/Entry = 4

TABLE A.9 The rate of erosion versus the impact velocity of SiC powder impacting the {001} in NaCl, KCl, and LiF, and the {111} in CaF₂. *

Material	Velocity (m/s)	Rate of Erosion (gm/s x 10 ⁻⁴)				
NaCl	30	2.6	2.3	2.5	2.6	2.5
	50	3.1	2.9	3.0	3.0	3.0
	70	3.7	4.0	3.7	4.1	3.8
	100	5.0	4.9	4.9	4.9	4.9
	120	5.5	5.6	5.4	5.5	5.4
KCl	30	1.8	1.7	1.6	1.6	1.7
	50	2.3	2.1	2.1	2.3	2.2
	70	3.2	3.1	3.2	3.2	3.2
	100	4.4	4.7	4.4	4.6	4.5
	120	5.1	4.6	5.0	5.0	4.9
LiF	30	3.1	3.5	3.4	3.4	3.5
	50	4.3	4.0	4.1	4.2	4.2
	70	5.1	4.7	4.7	4.8	4.9
	100	6.4	5.5	5.8	5.6	5.6
	120	7.4	6.2	6.3	6.3	6.5
CaF ₂	30	3.0	3.0	3.1	3.0	3.0
	50	4.4	4.2	4.0	4.1	4.3
	70	5.0	4.5	4.6	4.5	4.5
	100	5.1	5.0	5.5	5.0	5.2
	120	5.9	6.2	5.9	5.8	5.8

* Number of Samples/Entry = 4

LIST OF REFERENCES

LIST OF REFERENCES

1. S. M. Wiederhorn and D. E. Roberts, "A Technique to Investigate High Temperature Erosion of Refractories," Am. Ceram. Soc. Bull., 55 [2], 185-189 (1976).
2. C. M. Preece and N. H. MacMillan, "Erosion," in Ann. Review of Material Science, edited by R. A. Huggins, R. H. Bube, and R. W. Roberts, Annual Reviews, Inc., Palo Alto, CA, 1977.
3. B. Vyas and C. M. Preece, "Cavitation of Face Centered Cubic Metals," Met. Trans. A, 8A [6], 915-923 (1977).
4. D. W. Budworth, An Introduction to Ceramic Science, Pergamon Press, New York, 1970.
5. J. J. Gilman, "Plastic Anisotropy of Lithium Fluoride and Other Rock-Salt Type Crystals," Acta Metall., 7, 608-613 (1959).
6. J. J. Gilman and W. G. Johnson, "Dislocations in LiF Crystals," Solid State Physics, 13, 148-156 (1962).
7. J. J. Gilman and W. G. Johnson, "Observations of Dislocation Glide and Climb in LiF," J. Appl. Phys., 27 [9], 1018-1022 (1962).
8. T. L. Johnston, C. H. Li, and R. J. Stokes, "The Strength of Ionic Solids," in Strengthening Mechanisms in Solids, ASM, Metals Park, OH (1962).
9. R. E. Keith and J. J. Gilman, pp. 3-19 in Symposium on the Basic Mechanisms of Fatigue, ASTM Spec. Tech. Publ., 1959, No. 237.
10. D. Hoover and J. Washburn, "Tensile Behavior of LiF," J. Appl. Physics, 33 [1], 11-18 (1962).
11. J. J. Gilman, C. Knudsen, and W. P. Walsh, ibid., 29 [4], 601-607 (1958).
12. K. N. Subramanian, "Work Hardening and Deformation Structure in Lithium Fluoride Single Crystals," PhD Thesis, Michigan State University, East Lansing, MI, 1966.
13. T. McGuinness and A. Thiruvengadam, pp. 30-35 in Erosion, Wear, and Interfaces with Corrosion, ASTM Spec. Tech. Publ., 1974, No. 567.

14. G. S. Springer and C. B. Baxi, pp. 106-127 in Ref. 13.
15. M. C. Rochester and J. H. Brunton, pp. 128-151 in Ref. 13.
16. A. F. Conn and S. L. Rudy, pp. 239-269 in Ref. 13.
17. D. E. Elliott, J. B. Marriott, and A. Smith, pp. 127-161 in Characterization and Determination of Erosion Resistance, ASTM Spec. Tech. Publ., 1970, No. 474.
18. W. D. Pouchot, pp. 383-408 in Ref. 17.
19. P. Eisenberg, pp. 3-28 in Ref. 17.
20. M. S. Plesset and R. E. Devine, "Effect of Exposure Time on Cavitation Damage," J. Basic Eng., Trans. ASME, 88D [4] 691-705 (1966).
21. G. Hoff, G. Langbein, and H. Rieger, pp. 42-55 in Ref. 17.
22. B. J. Hockey, S. M. Wiederhorn, and H. Johnson. "Erosion of Brittle Materials by Solid Particle Impact," NBSIR 77-1396 (1977).
23. F. Erdmann-Jesnitzer and H. Louis, pp. 171-196 in Ref. 13.
24. B. Vyas and C. M. Preece, pp. 77-105 in Ref. 13.
25. P. Ascarelli, US Army Mater. Mech. Res. Cent. Tech. Rep. No. 71-47 (1971).
26. C. E. Smeltzer, M. E. Gulden and W. A. Compton, "Mechanisms of Metal Removal by Impacting Dust Particles," J. Basic Eng., Trans. ASME, 92D, 639-654 (1970).
27. P. A. Engel, Impact Wear of Materials, Elsevier Scientific Publishing Co., Amsterdam, 1976.
28. I. Finnie, "Some Observations on the Erosion of Ductile Metals," Wear, 19, 81-90 (1972).
29. G. P. Tilly, "A Two Stage Mechanism of Ductile Erosion," ibid., 23, 87-96 (1973).
30. R. E. Winter and I. M. Hutchings, "Similarities and Differences in the Erosion Behavior of Materials," ibid., 25, 141-148 (1975).
31. G. L. Sheldon, "Similarities and Differences in the Erosion Behavior of Materials," J. Basic Eng., Trans. ASME, 62D, 619-626 (1970).
32. I. Finnie, "Erosion of Surfaces by Solid Particles," Wear, 3, 87-103 (1960).

33. H. Hertz, "Ueber die Berührung Fester Elastischer Körper," J. Reine Angew. Math., 92, 156-171 (1882).
34. L. B. Greszczuk, pp. 183-211 in Foreign Object Impact Damage to Composites, ASTM Spec. Tech. Publ., 1975, No. 568.
35. F. B. Langitan and B. R. Lawn, "Hertzian Fracture Experiments on Abraded Glass Surfaces as Definitive Evidence for an Energy Balance Explanation of Auerbach's Law," J. Appl. Physics, 40 [10] 4009-4017 (1969).
36. B. R. Lawn and T. R. Wilshaw, "Indentation Fracture: Principles and Applications," J. Mater. Sci., 10 [1] 113-122 (1975).
37. B. R. Lawn, E. R. Fuller, and S. M. Wiederhorn, "Strength Degradation of Brittle Surfaces: Sharp Indenters," J. Mater. Sci., 59 [5-6] 193-197 (1976).
38. F. B. Langitan and B. R. Lawn, "Effect of a Reactive Environment on the Hertzian Strength of Brittle Solids," J. Appl. Physics, 42 [13] 5540-5545 (1971).
39. A. G. Evans, "Strength Degradation by Projectile Impacts," J. Am. Ceram. Soc., 56 [8] 405-409 (1973).
40. B. R. Lawn and M. V. Swain, "Microfracture Beneath Point Indentations in Brittle Solids," J. Mater. Sci., 10 [1] 113-122 (1975).
41. B. R. Lawn, "Hertzian Fracture in Single Crystals with the Diamond Structure," J. Appl. Physics, 39 [10] 4828-4836 (1968).
42. B. R. Lawn, S. M. Wiederhorn, and H. H. Johnson, "Strength Degradation of Brittle Surfaces: Blunt Indenters," J. Am. Ceram. Soc., 58 [9-10] 428-432 (1975).
43. S. M. Wiederhorn and B. R. Lawn, "Strength Degradation of Glass Resulting from Impact with Spheres," ibid., 60 [9-10] 451-458 (1977).
44. F. C. Frank and B. R. Lawn, "Theory of Hertzian Fracture," Proc. R. Soc. London, Ser. A., 299 [1458] 291-306 (1967).
45. W. F. Adler, pp. 294-315 in Ref. 13.
46. A. W. Ruff and L. K. Ives, "Measurement of Solid Particle Velocity in Erosive Wear," Wear, 35, 195-199 (1975).
47. D. R. Pande and T. S. Murty, "Mechanism for the Formation of {100} Slip Lines Around a Dynamical Indentation on {100} Faces of Sodium Chloride Single Crystals," J. Phys. D., 7 [3] 403-406 (1974).

48. J. J. Gilman, "Hardness of Pure Alkali Halides," J. Appl. Phys., 44 [3] 982-984 (1973).
49. R. W. Armstrong and C. Cm. Wu, "Lattice Misorientation and Displaced Volume for Microhardness Indentations in MgO Crystals," 61 [3-4] 102-106 (1978).
50. A. S. Keh, "Dislocations in Indented Magnesium Oxide Crystals," J. Appl. Phys., 31 [9] 1538-1545 (1960).
51. J. R. Patel and B. H. Alexander, "Plastic Deformation of Germanium in Compression," Acta Metall., 4 [4] 385-395 (1956).
52. W. L. Phillips, Jr., "Deformation and Fracture Processes in Calcium Fluoride Single Crystals," 44 [10] 499-506 (1961).